Deep seismic imaging of the eastern Nankai trough, Japan, from multifold ocean bottom seismometer data by combined travel time tomography and prestack depth migration

J.-X. Dessa, S. Operto, S. Kodaira, A. Nakanishi, G. Pascal, K. Uhira, Y. Kaneda

Deep seismic imaging of the eastern Nankai trough, Japan, from multifold ocean bottom seismometer data by combined travel time tomography and prestack depth migration

J.-X. Dessa,[1] S. Operto,[1] S. Kodaira,[2] A. Nakanishi,[2] G. Pascal,[3] K. Uhira,[4] and Y. Kaneda[2]

Received 15 July 2003; revised 18 November 2003; accepted 15 December 2003; published 28 February 2004.

[1] The easternmost segment of the Nankai trough remained unruptured during the 1944 and 1946 earthquakes that affected the rest of the trench. It is therefore a zone of seismic gap that also undergoes a peculiar tectonic regime due to its proximity with the Izu collision zone. We investigate this area with densely sampled active seismic data. One hundred ocean bottom seismometers, spaced only 1 km apart, were deployed along a line perpendicular to the trough. A two-step tomographic approach, designed for this type of acquisition, is applied: first, a long-wavelength velocity model is built by a linearized inversion of first arrival travel times, its resolution is assessed, and its reliability is confirmed through a semiglobal approach in which a large range of starting models is tested; second, this tomographic model is used to exploit late reflected arrivals with a prestack depth migration, the result of which is validated by classically modeling refraction and reflection travel times in the derived structural model. Thus both velocities and discontinuities are mapped in our model with a minimum of data interpretation and a priori knowledge. Our results bring new insights on the deep crustal zones of the margin and its evolution. The existence of presently inactivated major thrusts is very clearly evidenced in the backstop. A general timing for its evolution and deformation is proposed. Farther seaward, the presence of a subducted ridge beneath the accretionary wedge is confirmed. Its compressive structure and origin are demonstrated. It exhibits a thickened lower crust which nature is discussed. Besides, strong analogies between this ''Paleo-Zenisu'' subducting ridge and the Zenisu ridge, observed farther south, are also emphasized, bringing evidences for a steady state crustal deformation pattern. *INDEX TERMS:* 0935 Exploration Geophysics: Seismic methods (3025); 3025 Marine Geology and Geophysics: Marine seismics (0935); 7220 Seismology: Oceanic crust; 8105 Tectonophysics: Continental margins and sedimentary basins (1212); 8180 Tectonophysics: Tomography; *KEYWORDS:* eastern Nankai Trough, wide-angle crustal seismic imaging, travel time tomography, prestack depth migration

Citation: Dessa, J.-X., S. Operto, S. Kodaira, A. Nakanishi, G. Pascal, K. Uhira, and Y. Kaneda (2004), Deep seismic imaging of the eastern Nankai trough, Japan, from multifold ocean bottom seismometer data by combined travel time tomography and prestack depth migration, *J. Geophys. Res.*, *109*, B02111, doi:10.1029/2003JB002689.

1. Introduction

[2] The Nankai trough is the boundary that marks the subduction of the Philippine Sea plate beneath the Japanese arc, that can kinematically be related to the Eurasian plate in first approximation. It extends over about 700 km, roughly between 133° and 139°E in longitude and between 31° and 34°N in latitude (Figure 1a). It is characterized by the occurrence of large subduction earthquakes whose direct (shaking) and indirect (tsunamis) consequences are potentially devastating for the densely populated regions they can affect. This explains the great scientific interest in this area and the considerable number of studies that were dedicated to it.

[3] The kinematics of the Philippine Sea plate with respect to Eurasia on the Nankai trough indicates a convergence of ~4.5 cm/yr at N310° [*Seno et al.*, 1993; *Mazzotti et al.*, 2000]. The seismic activity is characterized by the periodic rupture of well-identified segments of the trough [*Ando*, 1975b; *Cummins et al.*, 2002]. Historic documents dating back to the 7th century show that recurrence periods

[1]Géosciences Azur, CNRS UMR 6526, Observatoire Océanologique de Villefranche, Villefranche-sur-Mer, France.
[2]Institute for Frontier Research on Earth Evolution, Japan Marine Science and Technology Center, Yokohama, Japan.
[3]Laboratoire de Géologie, CNRS UMR 8538, École Normale Supérieure, Paris, France.
[4]Japan Meteorological Agency, Tokyo, Japan.

0148-0227/04/2003JB002689$09.00

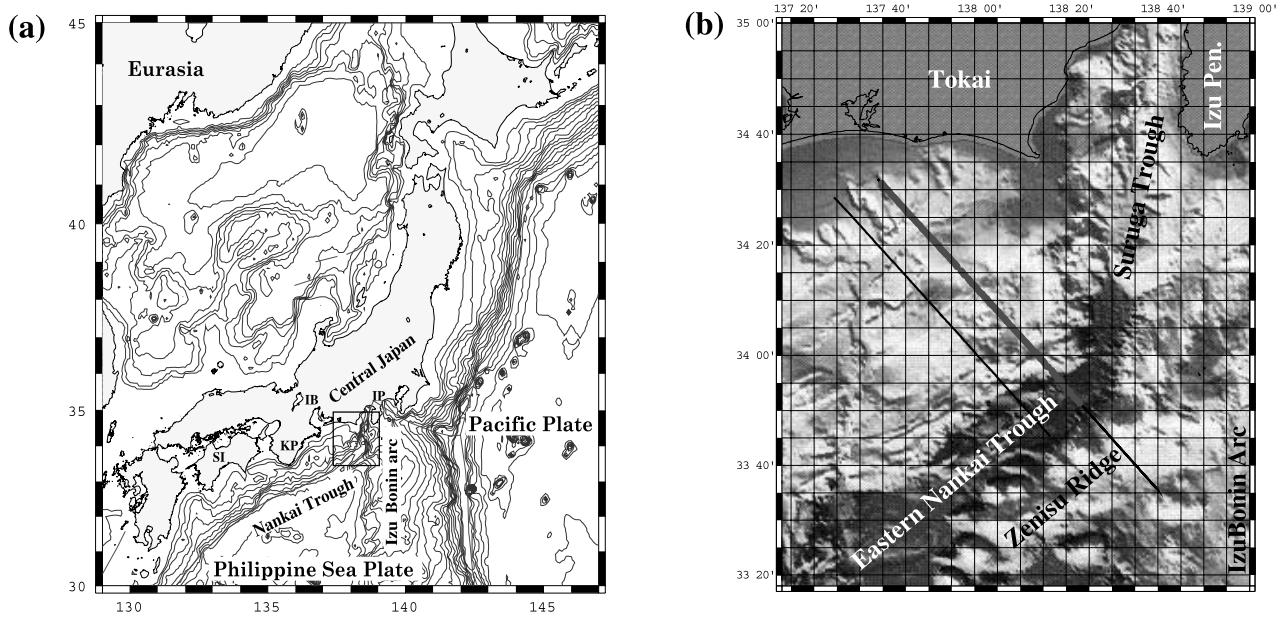

Figure 1. (a) General geodynamic setting around the Nankai trough (map after *Mazzotti* [1999]). Places referred to in the text as Shikoku Island, Kii Peninsula, Ise Bay, and Izu Peninsula are denoted SI, KP, IB, and IP, respectively. (b) Zoom of box shown in Figure 1a with the main structures of the survey area. The two straight black lines denote the shot profiles acquired during the survey; only data from the easternmost one are considered in this study. The thicker and shorter line superimposed on it corresponds to the OBS array. See color version of this figure at back of this issue.

are 100–200 years and that various rupture patterns are recorded, depending on the involved fault segments [*Ando*, 1975b; *Kumagai*, 1996]. In particular, some earthquakes rupture the whole trough from western Shikoku to the Tokai district (1707), whereas others only rupture eastern (1498, 1944) or western (1361, 1946) parts of the trough; the 1854 rupture consisted of a duplex in which both parts ruptured within a few hours.

[4] From a structural point of view, this segmentation of the margin is often corroborated by the existence of lateral discontinuities that possibly act as barriers to the lateral expansion of the coseismic rupture. Irregular subducting plate geometry around the southern end of Kii peninsula [*Mochizuki et al.*, 1998; *Sato et al.*, 1998; *Cummins et al.*, 2002] and beneath Ise bay [*Ishida*, 1992; *Sagiya and Thatcher*, 1999; *Nakanishi et al.*, 2002b] or the existence of a subducting seamount south of Shikoku island [*Yamazaki and Okamura*, 1989; *Kodaira et al.*, 2000] are likely to be such structures (Figure 1a). The irregularity in ruptured segments, however, shows that these barriers can occasionally be crossed, like in the 1707 event. In the light of this, the knowledge of structural variations of the margin appears to be of crucial importance in assessing the magnitude and rupture pattern of great earthquakes to come and evaluating their consequences.

[5] During the 20th century, where the development of recording instruments allowed a better estimation of the coseismic rupture characteristics in time and space, the Nankai trough was ruptured by the two large earthquakes of Tonankai (1944) and Nankaido (1946) that affected the eastern and western parts, respectively, of the trough with respect to the Kii peninsula. These two events were the subject of numerous studies based on seismological data [*Kanamori*, 1972; *Obana et al.*, 2001; *Cummins et al.*, 2002], geodetic data [*Thatcher*, 1984; *Satake*, 1993; *Sagiya and Thatcher*, 1999] and tsunami data [*Ando*, 1982; *Satake*, 1993; *Tanioka and Satake*, 2001; *Baba et al.*, 2002]. They released the accumulated stress on the widest part of the trough. The easternmost segment of the Nankai subduction system, including its termination in the Suruga trough, was, however, not affected by the 1944 event and therefore remains unruptured since the Ansei earthquake of 1854. This prompted some authors to conjecture about the future occurrence of a great subduction earthquake in this area where compressive stress has not been released for one and a half centuries [*Ando*, 1975a; *Le Pichon et al.*, 1996b].

[6] The eastern termination of the Nankai trough lies in a peculiar tectonic regime that is strongly influenced by the collision of the Izu-Bonin arc with central Japan, located just eastward (Figure 1b). The subduction happens to be locked around the Izu peninsula with a widely distributed compressive deformation within the colliding arc and northward on land [*Le Pichon et al.*, 1996a; *Mazzotti et al.*, 1999]. The easternmost segment of the Nankai trough thus marks the transition between this distributed deformation regime, which prevails eastward in the Izu-Bonin arc, and the more classical subduction westward, where the convergence is accommodated along the plate boundary through usual seismic cycles [*Lallemant et al.*, 1989; *Chamot-Rooke and Le Pichon*, 1989; *Mazzotti et al.*, 2002]. This transition zone is characterized by the existence of a compressive structure running parallel to the trench and located just seaward of it: the Zenisu ridge [*Lallemant et al.*, 1989;

Chamot-Rooke and Le Pichon, 1989] that can be seen in Figure 1b. A part of the convergence between the Philippine Sea plate (PHS) and central Japan (CJP), mainly oriented N-S and ranging between 10 and 19 mm/yr from its western to eastern end [*Mazzotti et al.*, 1999, 2001, 2002], is absorbed through this 2–3 km high topographic feature. The localization of the compressive tectonics presumably results from the reactivation of a paleotransform fault [*Mazzotti et al.*, 2002]. Hence the PHS/CJP convergence motion is partitioned between this intraplate N-S shortening on the Zenisu ridge and the subduction along the trench with axis oriented N290°–300°. The subduction velocity ranges between ~20 and ~30 mm/yr from east to west of the Zenisu-West Izu block, kinematically defined as a platelet located between the Zenisu ridge and the subduction front and including the adjacent western part of the Izu-Bonin arc [*Mazzotti et al.*, 1999; *Sagiya*, 1999; *Henry et al.*, 2001; *Mazzotti et al.*, 2001].

[7] The existence of the compressive tectonics that is responsible for the formation of the Zenisu ridge is directly related to the collision of the Izu peninsula with central Japan, since ~2 Ma [*Huchon and Kitazato*, 1984]. This collision is an episode of the PHS/CJP convergence that was preceded by several other analogous events dating as far back as 15 Ma [*Taira et al.*, 1989]. This prompted some authors [*Lallemand et al.*, 1992; *Le Pichon et al.*, 1996b] to propose the hypothesis of another ridge, comparable to the Zenisu ridge and therefore often referred to as the ''Paleo-Zenisu'' ridge, which would have been subducted and would presently be in contact with the backstop, beneath the accretionary prism developed by the eastern Nankai subduction system. It is even proposed that the formation and subsequent subduction of compressive ridges is periodical [*Mazzotti et al.*, 2002; *Kodaira et al.*, 2003]. The presence of a subducting crustal topographic high such as the Paleo-Zenisu ridge must have major consequences on the mechanical behavior of this eastern termination of the subduction, whether it is with regard to earthquake triggering or to the resultant rupture pattern. To characterize the existence of this structure and to assess its possible properties and effects, there is a need for sharp structural information in the deep part of the subduction, that is, in the oceanic crust located below the accretionary wedge and the backstop, and in the backstop itself; the geometry of the décollement that delineates the plate contact is also naturally of particular interest.

[8] To this end, a wide-angle seismic survey was acquired on the eastern Nankai trough, off Tokai district. The acquisition setting was designed to combine both a large range of offsets, like in classical wide-angle surveys, and a dense seismic coverage of the zone of interest, in the sense of what is usually performed through multichannel seismic data acquisition. This kind of geometry is expected to allow both a precise kinematic characterization of structures (*P* wave velocities), brought by postcritical reflected and refracted arrivals, and a focused and continuous imaging of discontinuities, from spatial density of data. We give a precise description of this seismic data acquisition device in the second part of our study. Our data processing consists of a two-step approach: a velocity model is derived from first arrival travel time tomography that is used for a prestack depth migration of data. The travel time tomography technique is developed in section 3. Section 4 presents the tomographic model obtained, with resolution and robustness analyses. The migration technique and results are presented in section 5, and section 6 discusses the results.

2. Data Acquisition

[9] The data presented and processed hereafter were acquired during the KY0106 cruise, performed by the Institute for Frontier Research on Earth Evolution between 29 July and 6 September 2001, by the R/V *Kaiyo*. In accord with the purpose of the survey, exposed in section 1, a dense array of 100 ocean bottom seismometers (OBSs) was deployed along a N314° oriented line, that is, in a direction roughly perpendicular to that of the subduction structures. A constant spacing of 1 km between these stations was observed, leading to a 100-km-long receiver line. This geometry appeared to offer the best compromise between large offset coverage and dense spatial coverage with respect to the targeted structures. Two shot profiles were performed with this array, one being coincident with the OBS line and the other being parallel, 20 km westward; we only deal with the former profile in the present study. This shot line is 140-km-long, with a 100-m spacing between successive shots (1404 shot positions). Practically, it was acquired in two boat passes, with 200-m-spaced staggered source positions, and the data were subsequently merged. With this procedure, the greater time delay between successive recordings diminishes noise from previous shots.

[10] The seismic source consists of an array of eight air guns, each one featuring a 1500 cubic inch volume; the total volume of the source is 196 L. Shot positions were controlled by differential GPS. The OBSs, provided by the Japan Marine Science and Technology, are equipped with a three-component geophone (4.5 Hz) and a hydrophone [*Shinohara et al.*, 1993]. Their sampling rate is 10 ms, and their positioning is controlled through a Super Short Base Line system, with a depth accuracy of 2–3%. Three of the OBSs were not recovered. Among the others, 91 provided exploitable data. In this study, we only deal with the vertical component data from the geophones rather than those of the hydrophones that appear to be of poorer quality.

[11] Three examples of OBS gathers are displayed in Figure 2. The data were preprocessed with a minimum phase spectral deconvolution (whitening), a Butterworth band-pass filtering (3 and 13 Hz for cutoff frequencies); an automatic gain control (AGC) was applied and finally, a spectral matrix filtering. Spectral whitening efficiently removed ringing effects caused by the narrow frequency band of the source signature at the expense of signal-to-noise ratio that was reimproved by the subsequent band-pass filtering and spectral matrix filtering. The latter consists in projecting the signal on the main eigenvectors of the frequency domain cross-correlation matrices in order to separate the coherent signal from uncorrelated noise.

[12] Several phases can be distinguished, among which refracted and reflected waves are identified. Note the strong lateral variation between arrivals recorded along the profile

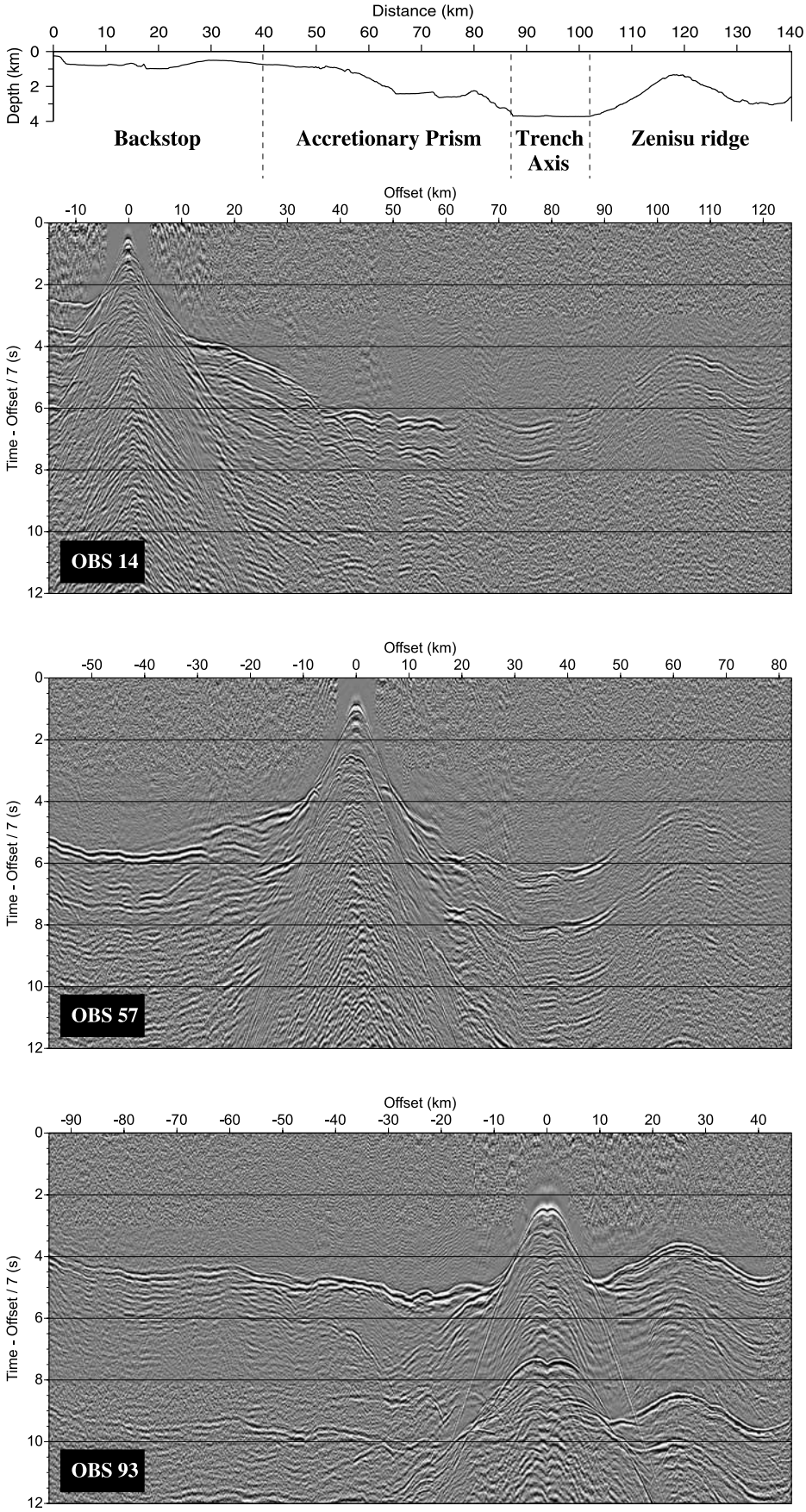

Figure 2. Example of three OBS gathers (14, 57, and 93). The position of the OBSs with respect to the structures of the margin is given on the top panel.

(Figure 2) that illustrates the complexity of the medium. In this study, we only refer to *P* wave arrivals.

3. Linearized Travel Time Tomography

[13] The tomographic approach that we applied to the data set is a first arrival travel time fitting procedure. First arrivals are picked in data and a model is searched for whose computed first arrivals match the observed ones. These synthetic travel times are computed on a grid that maps the model space through a finite difference resolution of the eikonal equation [*Vidale*, 1988; *Podvin and Lecomte*, 1991; *Hole and Zelt*, 1995]. The process is cast in an inverse problem formalism in which an objective function that quantifies the data fit is defined and minimized. This approach is significantly different from the classical wide-angle data processing based on a layer stripping procedure. Neither any phase identification, nor any a priori knowledge, such as a given number of layer, are required. In this sense, the technique can be considered as objective and robust, first arrival travel time picking errors being the only potential source of mistake in terms of input information. On the other hand, the handled amount of information is less since only first arrivals are being fit and no multivalued travel times are considered, in particular from reflected phases. This yields smooth models whose resolution is limited to the first Fresnel zone [*Williamson*, 1991], the width of which increases with large offsets.

[14] The strategy to solve the travel time fitting inverse problem is a linearized approach of local and iterative convergence initiated from a starting model. At each iteration, travel time tables are computed using a finite difference eikonal equation solver [*Hole and Zelt*, 1995]. For a given source-receiver pair j, the travel time is given by

$$t_j = \int_{\Gamma_j} u \, dl, \tag{1}$$

with Γ_j, the ray path along which time is integrated and u, the model slowness. Ray paths are computed from travel time tables by discrete back propagation along the travel time gradient direction, for each source-receiver pair. Considering such a segmented ray, equation (1) becomes

$$t_j = \sum_i u_i \, \delta l_i, \tag{2}$$

where i stands as an index over ray segments, u_i being the slowness at the middle of each one.

$$\frac{\partial t_j}{\partial u_i} = \delta l_i \tag{3}$$

simply derives from equation (2).

[15] In a tomographic inverse problem, one wishes to update a slowness model in order to fit observed travel times. This requires a model parameterization space to be defined and a sensitivity kernel $\mathcal{F}$, that maps this model space to the data space, to be computed. A Cartesian parameterization grid is defined by decimating the travel time modeling grid. Partial derivatives of time, which are known at the middle of ray segments, have to be expressed on the nodes of this grid. This is achieved by distributing the values derived from equation (3) on the four points of the inversion grid that define the cell containing the corresponding ray segment. The slowness interpolation scheme used to do so is that of *Thurber* [1983, equation (2)].

[16] Once the Fréchet derivative matrix $\mathcal{F}$ is obtained, the inverse problem is cast as the following sparse linear system [*Toomey et al.*, 1994]:

$$\begin{pmatrix} \mathcal{C}_d^{-1/2}\Delta\mathbf{t}^{(k)} \\ 0 \\ 0 \end{pmatrix} = \begin{pmatrix} \mathcal{C}_d^{-1/2}\mathcal{F} \\ \lambda_h \mathcal{S}_h \\ \lambda_v \mathcal{S}_v \end{pmatrix} \left(\Delta\mathbf{m}^{(k)}\right), \tag{4}$$

in which $\mathcal{S}_h$, $\mathcal{S}_v$ are horizontal and vertical Gaussian smoothing matrices [*Toomey et al.*, 1994], $\mathcal{C}_d$ the covariance matrix of data uncertainties; λ_h and λ_v are scalars that control the balance between these imposed constraints and that of data fitting. $\Delta\mathbf{m}$ denotes the model perturbation and k is the iteration index. The system is solved iteratively with a LSQR algorithm [*Paige and Saunders*, 1982]. Smoothing constraints are applied to avoid unphysical ray trappings in high-velocity spots that cause or increase the heterogeneity of ray coverage in models.

[17] The general linearized tomographic approach is quite similar to those of *Toomey et al.* [1994]; *Zelt and Barton* [1998]; *Korenaga et al.* [2000].

4. Travel Time Tomography Results

4.1. Travel Time Picking

[18] First arrival travel times are picked after a preprocessing step consisting of applying a band-pass filter and AGC to the data. For this purpose, we developed a semi-automatic picking procedure: first arrivals are manually picked for about one trace out of 10 on each OBS gather (the required picking density actually depends on the linearity of the associated travel time curve); these picked arrivals are interpolated; an intercorrelation is then performed between traces to be automatically picked and the closest manually picked one; the selected first arrival time corresponds to this closest picked time to which the delay of maximum intercorrelation is added, within the limits of a small time window centered on the interpolated time. Practically, for an OBS gather, picked travel times are separated between various offset windows within which the first arrival waveforms are coherent and the signal-to-noise ratio is homogeneous. Interpolation and cross correlations are performed separately for each of these windows that are characterized by a given level of picking error. We define and compute picking errors as the mean difference between interpolated travel times and their actual values (inferred from cross correlations); a systematic error corresponding to half of the signal dominant period is eventually added for phases with large offsets and poor signal-to-noise ratio for which an ambiguity exists concerning the polarity of the event to be picked.

4.2. Tomographic Inversion

[19] The tomographic approach is a linearized inversion that requires an initial model. This model is built by introducing a priori geological information concerning the general shape of the subduction as it was evidenced and

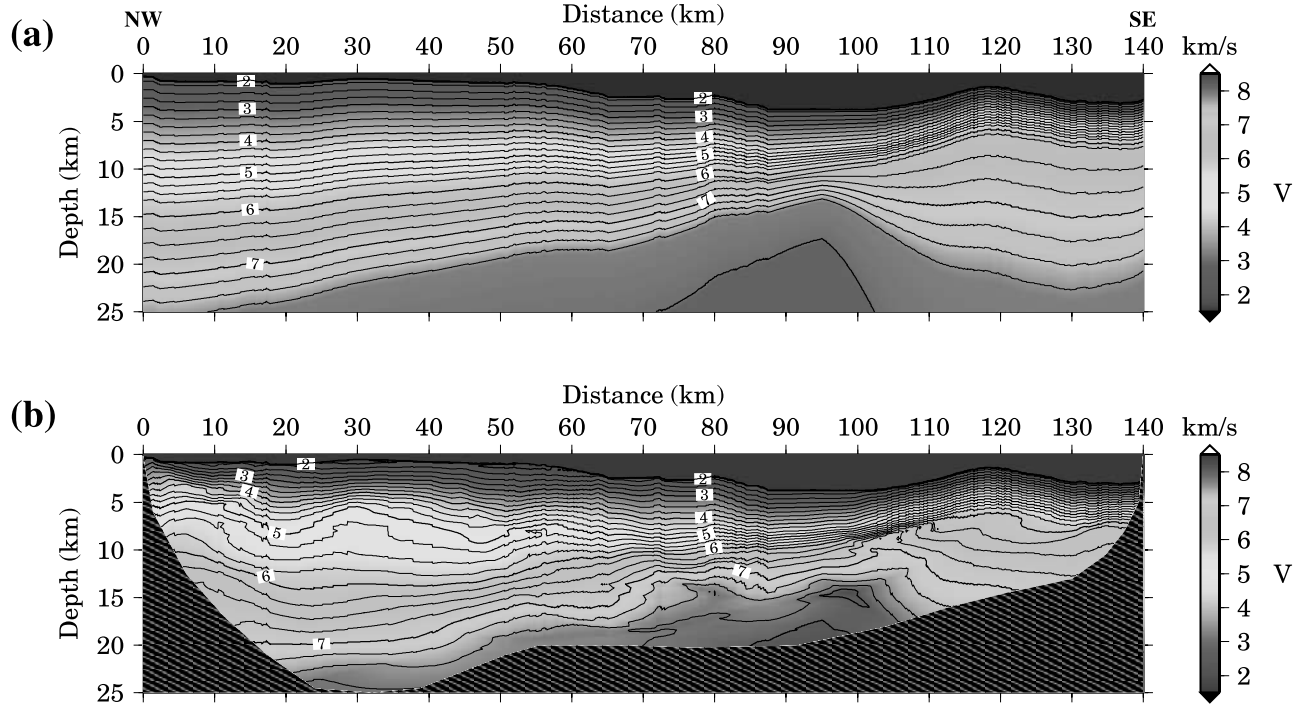

Figure 3. Result of tomographic inversion. (a) Starting model. (b) Corresponding output. The hachured pattern corresponds to unconstrained areas that are not covered by ray paths. See color version of this figure at back of this issue.

constrained by previous studies [*Mazzotti et al.*, 2002; *Takahashi et al.*, 2002; *Kodaira et al.*, 2003]. This model is displayed in Figure 3a.

[20] Once the initial model is obtained, picked first arrivals are inverted with the tomographic tool described above. A smoothing procedure is defined in order to allow a minimization of the travel time misfit while keeping the smoothness of the model and, consequently, a relatively distributed ray coverage. This aim is achieved by progressively relaxing the smoothing constraint with Gaussian functions of decreasing correlation lengths as iterations proceed. For the first 5 iterations, Gaussian smoothers widths were set to 5 and 20 km for vertical and horizontal directions respectively. They were subsequently halved between iterations 6 and 10 and finally set to 2 and 8 km up to iteration 15. Meanwhile, the RMS misfit dropped from 0.56 s (starting model) to 0.11 s. Further iterating did not improve data agreement significantly even when the smoothing conditions kept on being relaxed but in this latter case, polluting ray prints appeared due to ray channeling.

[21] Figure 3b illustrates the resulting tomographic model of the eastern Nankai trough area. Ray coverage issues must be addressed in order to assess the reliability of retrieved features. An analysis of ray paths distribution shows that structures are illuminated down to 20 km in depth at the center of the model, and more superficially on its edges, particularly oceanward. This result is confirmed by the resolution analysis presented in section 4.3.

[22] The general structures of the subduction are easily identifiable in this tomographic model with a subducting oceanic plate, over which velocity patterns associated with the trench (from 85 to 105 km of horizontal distance), wedge (from 50 to 85 km or so) and backstop (landward of the latter) can be distinguished. The topographic high, just seaward of the trough, is the Zenisu ridge.

[23] The Zenisu ridge area is not ideally covered by our acquisition geometry since the OBS array ends just landward of it; only shot positions cover the area (Figure 1b). The tomographic model of Figure 3b is therefore likely to depend on the starting model regarding the velocity structure below the Zenisu ridge. This point is actually confirmed by initiating the inversion from different models as it is done in our robustness analysis, presented further. The local non-uniqueness of the solution results from the absence of short-offset data and thus from our not recording of shallow refracted arrivals which prevents the upper structures from being kinematically constrained; they instead remain essentially unchanged with respect to the starting model. This in turn yields a trade-off in deeper reconstructed velocities. In other words, the problem appears to be ill-posed regarding the Zenisu ridge area but this does not affect the other reconstructed structures, particularly those located landward of the trench fill which are more specifically targeted in this experiment. The robustness analysis confirms this point.

[24] Figure 4 represents the three OBS gathers of Figure 2 with superposition of corresponding travel time curves computed in our model. The fit between the onset of coherent events and the curves is fairly good over a wide range of offsets for each of these distant OBSs. A more exhaustive illustration of the decrease in residuals during the tomographic inversion for every source-receiver pair is given by Figure 5.

4.3. Resolution Analysis

[25] In order to assess the resolution scale that is reached in this tomographic inversion, a resolution analysis is made

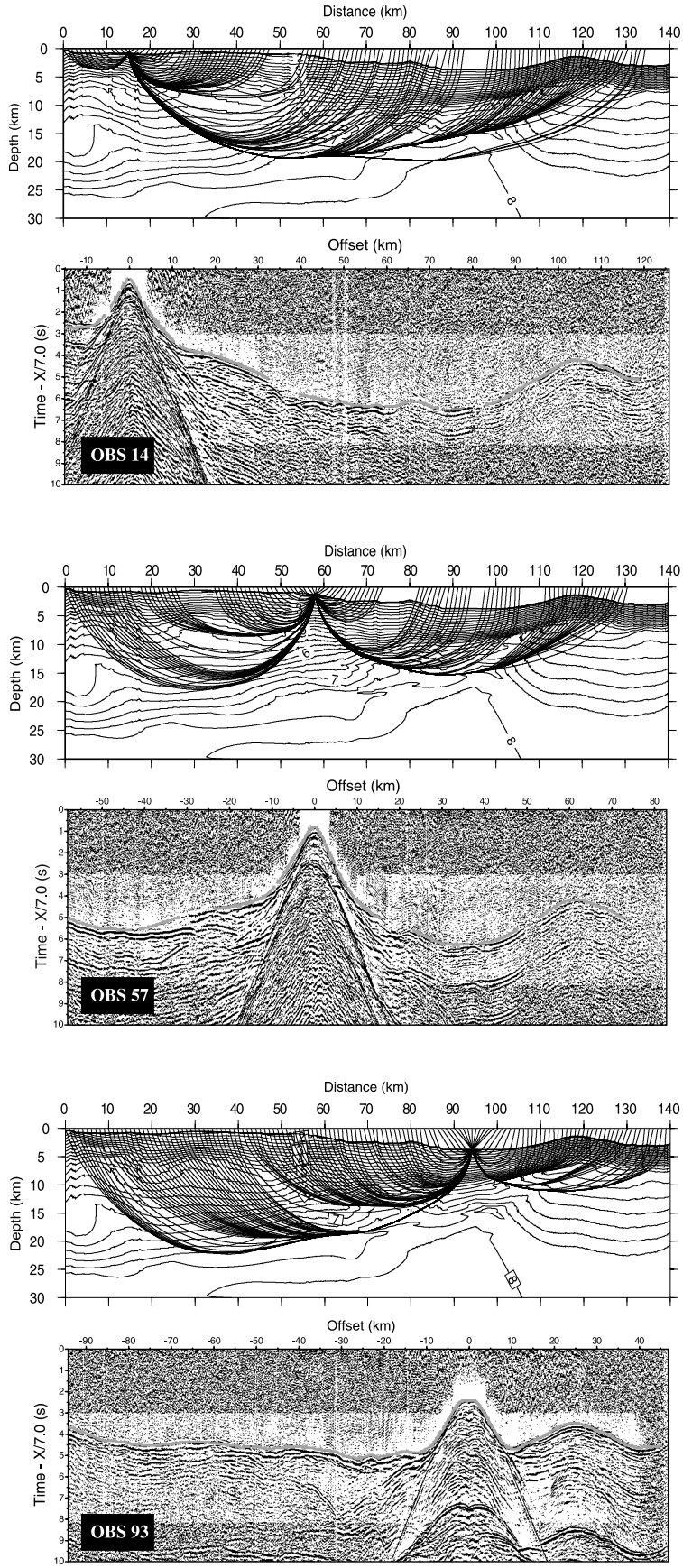

Figure 4. Data with first arrival travel time curves computed in our tomographic model for OBSs 14, 57, and 93. Corresponding ray fields are represented above each panel.

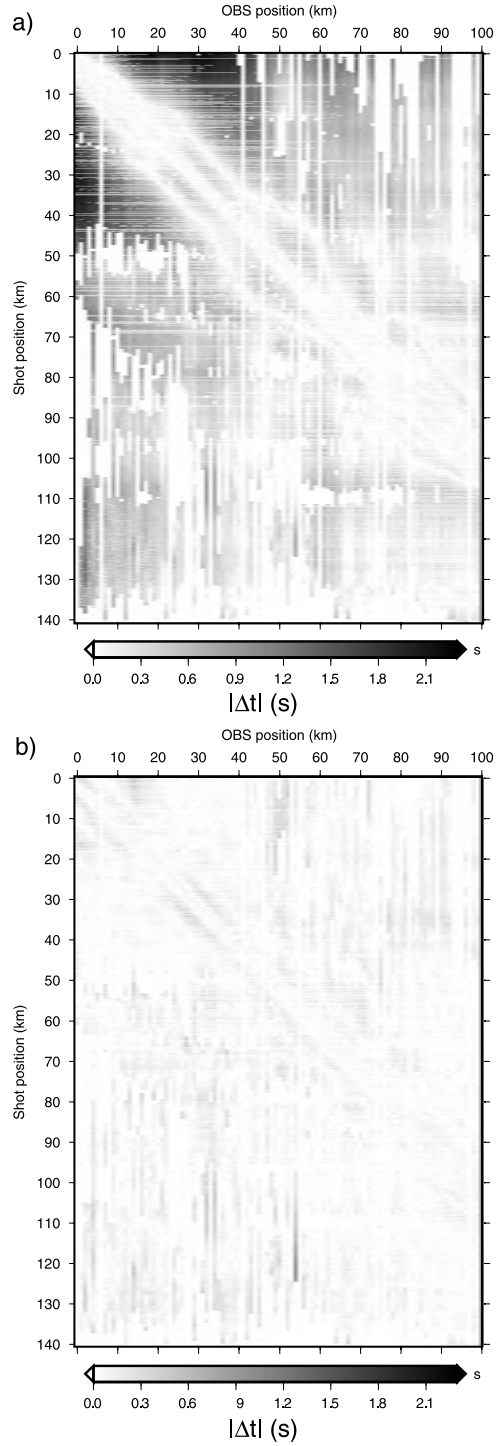

Figure 5. Absolute value of travel time residuals represented as a function of source and receiver positions. (a) Initial values corresponding to the starting model of Figure 3a. (b) Final values corresponding to our tomographic model.

with ''checkerboard'' tests [*Hearn and Ni*, 1994; *Zelt and Barton*, 1998]. A periodic square-patterned velocity anomaly featuring periodic positive and negative amplitudes is added to our tomographic model. Synthetic data are computed in these perturbed models and subsequently inverted, starting from the corresponding unperturbed models. The velocity anomaly is set to ±0.3 km/s and 2 inversions are carried out with 10 km and 5 km square anomalies. The results are presented in Figure 6. The 10 km square anomalies are generally well retrieved down to about 15 km. One can consider that only mean velocities can be constrained in deeper covered zones. The resolution is degraded in the backstop area where anomalies are distorted. The same kind of distortion is quite obvious beneath Zenisu ridge (beyond 110 km of horizontal distance). At the seaward end of the model, anomalies are not identifiable, which confirms our trade-off diagnosis between shallow and deeper structures in this zone. It can also be noticed that below 10 km in depth and beyond a distance of 60 km, reconstructed patterns have slightly overestimated velocity anomalies. Regarding the 5 km anomaly test, it can be observed that patterns are well retrieved down to 10 km in depth. Images are rapidly degrading below, particularly for the backstop area in the final model test. The pronounced stretching of the anomalies beneath Zenisu ridge, related to the peculiarity of our acquisition, is fairly visible.

[26] These tests show that a good resolution threshold is reached for structures above 10 km depth, except on both ends of the profile, especially seaward. Between 10 and 15 km depth, the horizontal resolution is degraded, only 10-km anomalies are still identified, because of a lack of angular coverage (only rays with direction close to horizontal cross the corresponding cells). Below 15 km, resolution is very poor and deep refracted rays only inform on the average properties of the structures they travel through.

4.4. Convergence and Error Analysis

[27] As already mentioned, our tomographic inversion belongs to the class of linearized inverse problems in that it requires a starting model that is iteratively updated through a sensitivity kernel. The solution of such a problem is likely to depend on this initial model, and, should the latter be too far from the real solution, the process may converge in a secondary minimum of the misfit function. To assess the robustness of our inverted model, we test its dependency on the starting model. This is done by initiating inversions from a class of models that we consider mapping a range of likely velocity distributions, following an approach comparable to that of *Korenaga et al.* [2000]. In order to do this, the starting model of Figure 3a is used. First bathymetry is removed. A set of five control profiles is defined at relevant distances, namely, 0 km, 140 km (ends of the model) and 65 km (accretionary wedge), 95 km (trench), 117 km (Zenisu ridge). On these profiles, independent stretching coefficients ranging between 0.7 and 1.4 are randomly generated and applied. The profiles are interpolated and yield models on which bathymetry is finally readded. One hundred of these random initial models are generated, and 5 tomographic iterations are carried out, starting from each of them, with the first step of our smoothing schedule (20 km horizontally and 5 km vertically). These first 5 iterations are actually sufficient to clearly retrieve the general features of the velocity distribution.

[28] Proceeding from 100 different initial models, we ended up with 100 tomographic models that can be compared. We computed average and maximum deviation models for both families of initial and final velocity models.

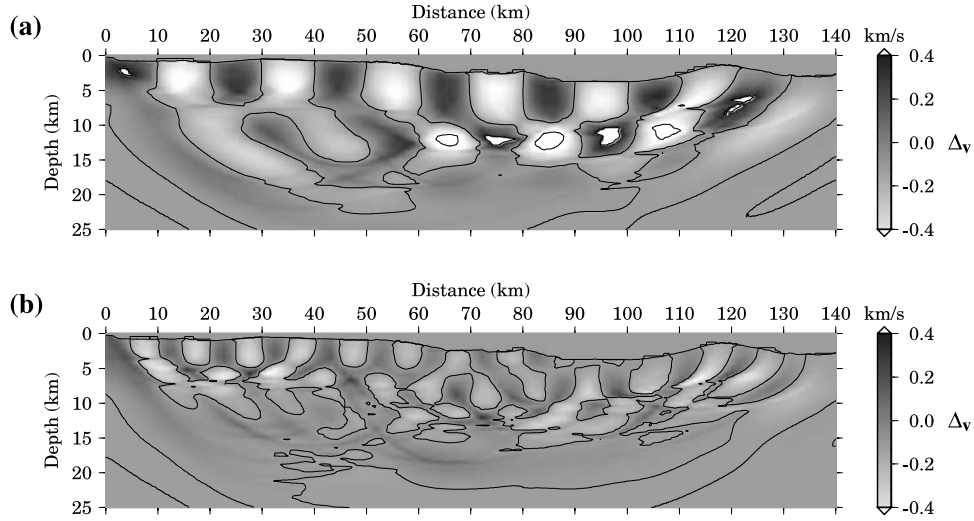

Figure 6. Results of "checkerboard" tests in the tomographic model of Figure 3b for (a) 10 km and (b) 5 km square anomalies.

Results are shown in Figure 7. The average model is computed by taking the mean values of the 100 final models at each point of the grid. We define the maximum deviation as the half width of the velocity intervals covered by our family of initial or final models, still for each point of the model parameterization grid. The comparison of results between Figures 7b and 7c shows quite clearly that the variability between models was substantially decreased in the process of travel time inversions, proving that noticeably different starting models yield a narrow range of final models around the average model of Figure 7a. Note that this average model is very similar to our model of Figure 3b. It is, however, less

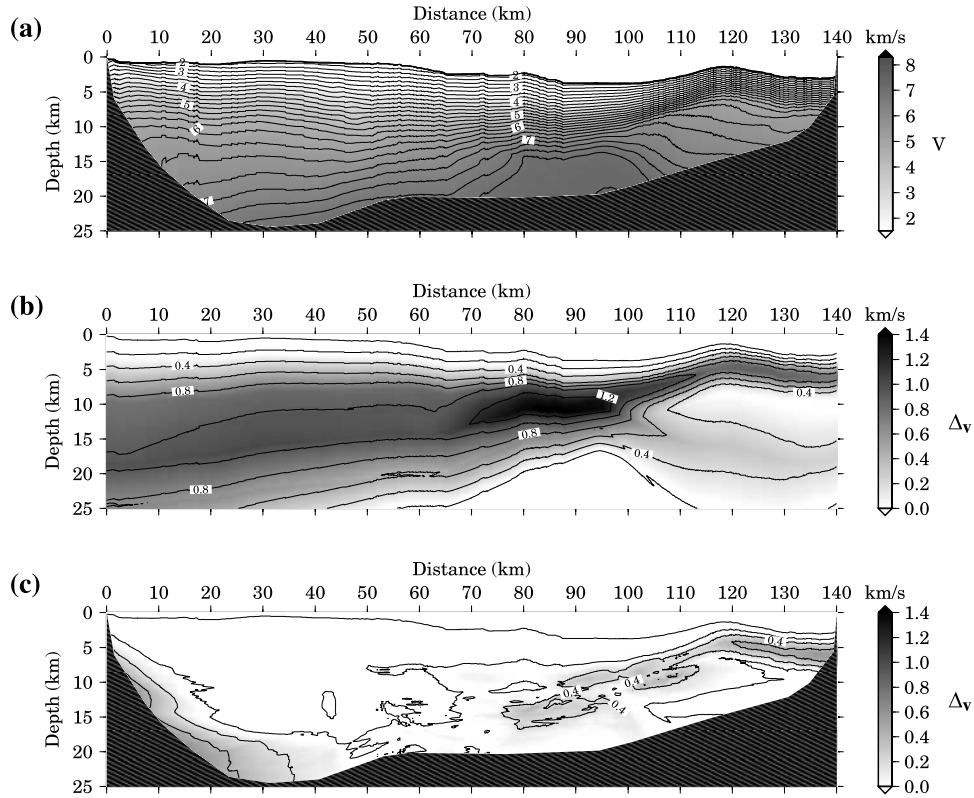

Figure 7. Results of the series of inversions initiated from a family of 100 randomly generated models. (a) Average tomographic model, built up with the mean velocities in the final models. (b) Maximum deviation in the initial models, defined as half of the velocity interval covered by the 100 models at each point of the grid. (c) Maximum deviation in the final models and error estimate on our tomographic model.

well resolved since it results from a summation over models that were themselves obtained with a small number of iterations and large-scale smoothing operators.

[29] This approach furthermore allows us to provide an estimate of the uncertainties that affect reconstructed velocities and therefore to assess their reliability by mapping associated errors. Most of the error model thus derived features a very small uncertainty, below 0.2 km/s. As we could expect, the largest uncertainties mainly concern the Zenisu ridge area. A shallow layer with errors of 0.4 km/s to more than 0.6 km/s is observable between ~120 km and 140 km. It perfectly corresponds to the lack of angular coverage in this area as only vertical rays cross the structures, due to the absence of close receivers. The variability between models is only partially decreased here during the tomographic process, meaning that a strong footprint of the starting model remains. The travel time delays between models that is acquired through this shallow, poorly constrained area is balanced at greater depth. One could therefore expect similar uncertainties in deeper areas of the ridge but since the balance is made over a much wider zone, the associated velocity variations are more limited. Elsewhere in the model, areas with noticable errors concern the landward border of the covered domain and some structures beneath the trough. Regarding the first zone, we consider that variability is a consequence of poor angular coverage, just as for Zenisu ridge; concerning errors beneath the trough, we consider them to balance travel time anomalies acquired by (1) some relatively shallow rays beneath the landward flank of Zenisu ridge and (2) some deep rays that mark the landward border of the covered domain. These two types of ray actually happen to travel beneath the trench (see ray paths for OBS 93 in Figure 4).

[30] From the data fitting point of view, statistics can also be made on the initial and final distributions of travel time agreement in our random model study. The mean value of the RMS error distribution was decreased from 0.81 to 0.17 s; its amplitude (difference between maximum and minimum encountered values) dropped from 1.35 to 0.08 s and the associated standard deviation, from 0.31 to 0.01 s.

5. Migration Results

[31] Travel time tomography as it is performed in our study only exploits a limited amount of information in recorded data, namely the first arrival travel times. This process yields a tomographic model that is kinematically well constrained but whose resolution is limited. This results from our not considering reflected phases that are sensitive to the sharp discontinuities of the medium.

[32] As we explained in section 1, we aim at taking advantage of the density of our acquisition geometry to image the studied area by exploiting information in data with a minimum a priori knowledge. This prompted us not to consider travel time tomography tools that make use of reflected phases because they rely on an interpretation of data that can be arduous and misleading in a complex and laterally heterogeneous model, as it is likely to be the case here.

5.1. Prestack Depth Migration

[33] To replace the reflective interfaces in a medium for which a precise and robust kinematic model is available, ray-based prestack depth migration is a method of choice. This class of tool is abundantly used in the processing of steep angle seismic data. However, their use is not restricted to this context and they can prove a valuable approach to wide-angle data processing too, as shown by previous studies on synthetic data [*Zelt et al.*, 1998; *McMechan and Fuis*, 1987], real land data [*McMechan and Fuis*, 1987; *Milkereit et al.*, 1990; *Simon et al.*, 1996], land/marine data [*Lafond and Levander*, 1995] and marine data [*Holbrook et al.*, 1994; *McIntosh et al.*, 2000; *Fliedner and White*, 2003]. In particular, imaging deep structures requires the use of strong postcritical reflected phases that are only recorded at large offset.

[34] The quality of prestack depth migration is improved when the fold in data is increased. This actually yields a greater continuity in the reconstructed image of reflectors and a better signal-to-noise ratio. In the frame of a wide-angle OBS experiment, the fold is defined by

$$f = \frac{L}{2\Delta\mathcal{O}}, \tag{5}$$

where $\Delta\mathcal{O}$ is the OBS spacing and L denotes the range of offset over which a particular reflection is observed.

[35] The main limitation to the application of migration techniques to classical marine OBS data is their sparse receiver geometry (large $\Delta\mathcal{O}$) that prevents a sufficient fold and thus creates spatial aliasing that leads to a discontinuous imaging of reflectors, smeared with artifacts [*Zelt et al.*, 1998]. A second limitation of the fold comes from the recording of a high-amplitude direct wave (propagating in the water layer) as well as strong shallow diffractions by ocean bottom receivers. These waves are arduous to filter by either f-k or τ-p processing and preclude deep reflections from being observed at short distances, thus limiting the range of offsets over which these reflections of strong interest can be exploited; this range L is actually essentially limited to postcritical incidences.

[36] In their study of a synthetic, crustal-scale, wide-angle seismic imaging experiment, *Zelt et al.* [1998] conclude that insufficient fold likely leads to aliased images for a receiver spacing greater than 2 km. This limit indeed depends on data quality, medium complexity, and on the range of depths one seeks to image precisely but it, however, gives a rough estimate of the required space sampling. Our receivers being 1 km spaced, a prestack depth migration of the outcoming data set seems quite adapted to exploit reflected arrivals and retrieve continuous features in the deep targeted structures. Note that considering the results of *Zelt et al.* [1998], good imaging conditions could even arguably be met with a receiver array about half as dense as the one used in this study but it should not be forgotten that we deal with both noisy real data and a complex medium. In any case, crustal imaging through migration related tools is quite demanding in terms of acquisition capacities. This requirement being fulfilled, migration appeared to represent a valuable complement to our tomographic approach although some difficulties in separating refracted and reflected wave fields are encountered, particularly for such an ocean bottom acquisition.

[37] Prestack depth migration classically consists in repositioning reflected events in depth. This repositioning is

made in accordance with the sum of travel times from the source to the reflective scatterer and from this scatterer back to the receiver [e.g., *McMechan and Fuis*, 1987]. To compute travel times and other ray-related parameters such as geometrical amplitude and slowness vector, a dynamic ray tracing computed in a smooth velocity model discretized by cardinal cubic B spline functions is used [*Lambaré et al.*, 1996]. Our prestack depth migration algorithm relies on a preserved amplitude, ray + Born formalism. The ray + Born migration algorithm has previously been described in detail by *Thierry et al.* [1999] in the context of usual multichannel seismic imaging. The reader is referred to that paper for a detailed description of the method. To briefly summarize, it is cast in the frame of least squares inverse theory [*Tarantola*, 1987; *Jin et al.*, 1992]. Weighted data residuals are spread out along an isotime surface in the distance-depth domain for each source-receiver pair. The weights account mainly for the geometrical amplitude, the source-receiver aperture and the two dimensionality of the imaging. The contributions of each elementary trace are finally stacked. They interfere destructively off the reflector position and fade away, whereas they sum themselves coherently at the reflector position, hence the importance of spatial density of data to migrate. The algorithm is generally used as a one iteration process like any migration. The output is theoretically an image of *P* wave velocity short-wavelength perturbations parameterized on a grid of point diffractors. This is the main difference with well-known Kirchhoff migration algorithms in which the output is parameterized as reflectivity on continuous interfaces. The reliability of inferred velocity contrasts indeed depends on the preservation of amplitudes of reflected events during the preprocessing of the data but in any case, a structural image of reflectors is at least obtained.

[38] A particular issue regarding the migration of wide-angle data is the phase shift existing between precritical and postcritical reflections which, for the sake of rigor, should be taken into account before stacking elementary contributions. The phase shift cannot be implemented in the ray tracing since it is computed in our smooth tomographic model in which no interface is explicitly described. The only way to incorporate the phase shift in the migration algorithm would therefore be to identify the critical incidence for each reflected phases in the data and to apply corrections to the data. This seems extremely arduous given the complexity of our data set and would contradict our choice of introducing no a priori knowledge in our processing. Furthermore, the main part of the energy stacked in large offset data comes from postcritical, wide-angle reflections so that the bias introduced by possibly stacking marginal precritical ones should be very limited. Finally, as we explain in section 5.2, we are not aiming at quantifying reflections but more simply at identifying them. For these reasons, the postcritical phase shift was not taken into account in our migration.

5.2. Processing Sequence and Results

[39] The preprocessing of data used in our prestack depth migration is the same as that applied to data displayed in Figure 2, and it is described in section 2. An attempt of fully preserved amplitude migration was made but the results were not satisfying. There are two reasons for this: (1) the fold, though being important for an ocean bottom acquisition, still remains too limited compared with multichannel seismic experiments to warrant reliable quantitative information; and (2) the inability of the ray + Born approach to correctly model/invert amplitudes for wide-angle reflections, which are precisely the events that contribute the most in the building of the migrated image here. The presence of noisy traces that create strong spurious migration smiles is a further important reason for the failure of amplitude preserved prestack depth migration although it could be overcome with a careful trace editing. For these reasons, the scope of prestack depth migration is reduced to obtaining a structural image of the deep structures in the margin. In other words, it is only kinematic. This does not require preservation of recorded amplitudes in the preprocessing of the data and the effect of noisy artifacts was minored through both a renormalization of amplitudes between traces by deconvolution and the application of an AGC. Migrating deconvolved data with no AGC yields similar results, though slightly degraded in terms of reflector continuity. Migrating data in which the water direct arrival had been attenuated by f-k filtering also leads to results close to those presented here (Figure 8a), for which data with offsets ranging between 1 km and 70 km were included in the migration. Smaller offsets are polluted by strong multiples, poorly coherent sedimentary arrivals and the water direct wave; greater ones generally only feature deep refracted phases that are not good to migrate. No time window was applied to the data, the separation of refracted and postcritical reflected waves being often impossible and the later unwanted multiples migrating out of the model. Once the data are migrated, the resulting section is post-processed with an AGC, to even amplitudes, a time domain band-pass filter, to remove very low frequency events attributed to the migration of refracted waves, and a spectral matrix coherency filter, to respectively strengthen lateral coherency of reflectors and improve signal-to-noise ratio, particularly in the weakly covered shallow sedimentary areas; a mute is also applied above the bathymetry.

[40] The migration result is shown on Figure 8. Several reflectors are visible down to 20 km in depth. Their tectonic significance is discussed in section 5.3. Noticable differences can be observed between these reflectors, some featuring longer wavelengths than others, specially when depth increases. There are two reasons for this: (1) seismic velocities increase with depth, hence an increase of seismic wavelengths; (2) wide-angle reflected data are recorded at large offsets and intrinsically migrate into stretched reflectors since they bear information on relatively low wave numbers of the model [*Wu and Toksöz*, 1987].

5.3. Validation of the Approach

[41] Prestack depth migration leads to the reconstruction of reflective discontinuities in the zone of study. Since much of the subsequent interpretation of structures relies on these results and since that class of technique is only seldom applied to wide-angle data, it appeared important to validate the reflective model and to make sure that migrated reflectors correspond to observable late arrivals in raw OBS data. Establishing a correspondence between events observed in time recordings of OBS gathers and a depth migrated section is not straightforward from a purely observational

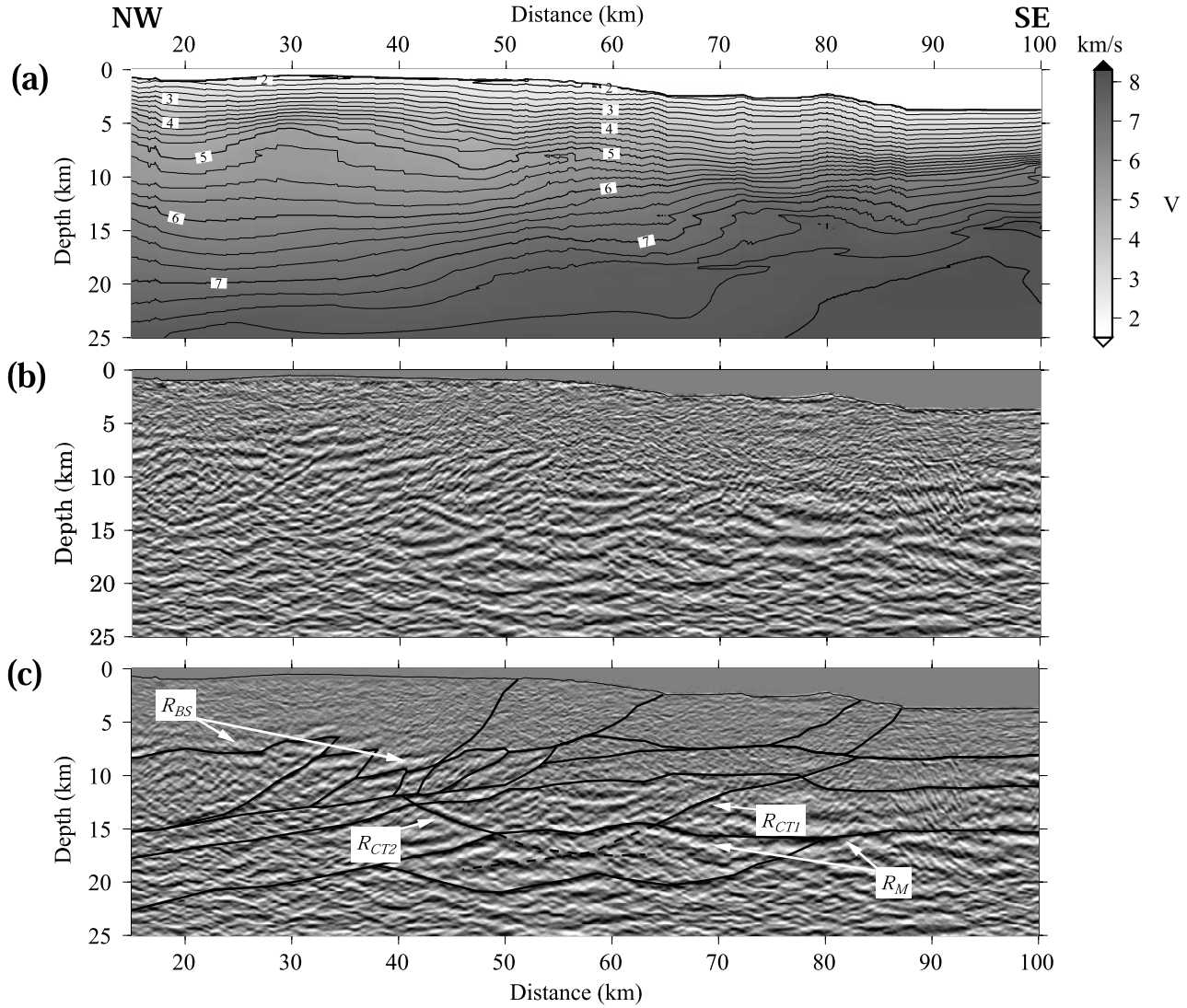

Figure 8. Result of prestack depth migration. (a) Tomographic model zoomed on the area corresponding to our migrated section, displayed below. (b) Migrated section. (c) Tectonic interpretation (see Figure 12) superimposed to migration result. Downward ends of R_{CT1} and R_{CT2} are unclear, hence the dashed line for their interpretation. The four shallowest reflectors affecting the prism are not based on our migration but on migration of coincident MCS data by *Martin* [2003].

point of view. Therefore we digitized our interpreted model (discussed in section 6) into a series of layers and floating reflectors and we used the velocities of our smooth tomographic model to build a blocky model of the studied area. This model was then used to compute travel times of both reflected and refracted arrivals corresponding to each of the defined layers, using the modeling approach of *Zelt and Smith* [1992]. The correlation can thus be made between migrated events and observed phases, to which an origin can furthermore be assigned. It is worth noting that this modeling is purely kinematic and does not account for the amplitude associated to any event. Therefore some modeled arrivals may have no correspondence everywhere in data but should at least have some over a limited range of offsets.

[42] A selection of 23 OBSs was made to check the relevance of the interpreted blocky model as well as its kinematic compatibility with the smooth model of Figure 3b. Results of the modeling are presented for 3 of these OBSs which respective numbers are 14, 57 and 93 (Figures 9, 10, and 11). Regarding OBS 14, the discontinuities interpreted as the top of the backstop and the Moho exhibit reflection travel time curves that clearly coincide with coherent arrivals in data, in particular close to critical distances. Reflections at the top and inside of the subducting oceanic crust correlate weakly with observed phases. It can be noted that the associated reflectors in the migrated section are poorly resolved at the indicated reflection distances. Travel times from the floating reflector associated with the first and main thrust in the backstop is exactly coincident with a strong arrival that can be better observed on the corresponding panel of Figure 2. Neighboring OBSs, not presented here, are also characterized by this event. On Figure 10, travel times are computed for reflections on the base of oceanic layer 3, crustal discontinuity (layer 2 to layer 3), top of the crust and top of the backstop continued (from 55 to 67 km of distance) along a small bulge-shaped

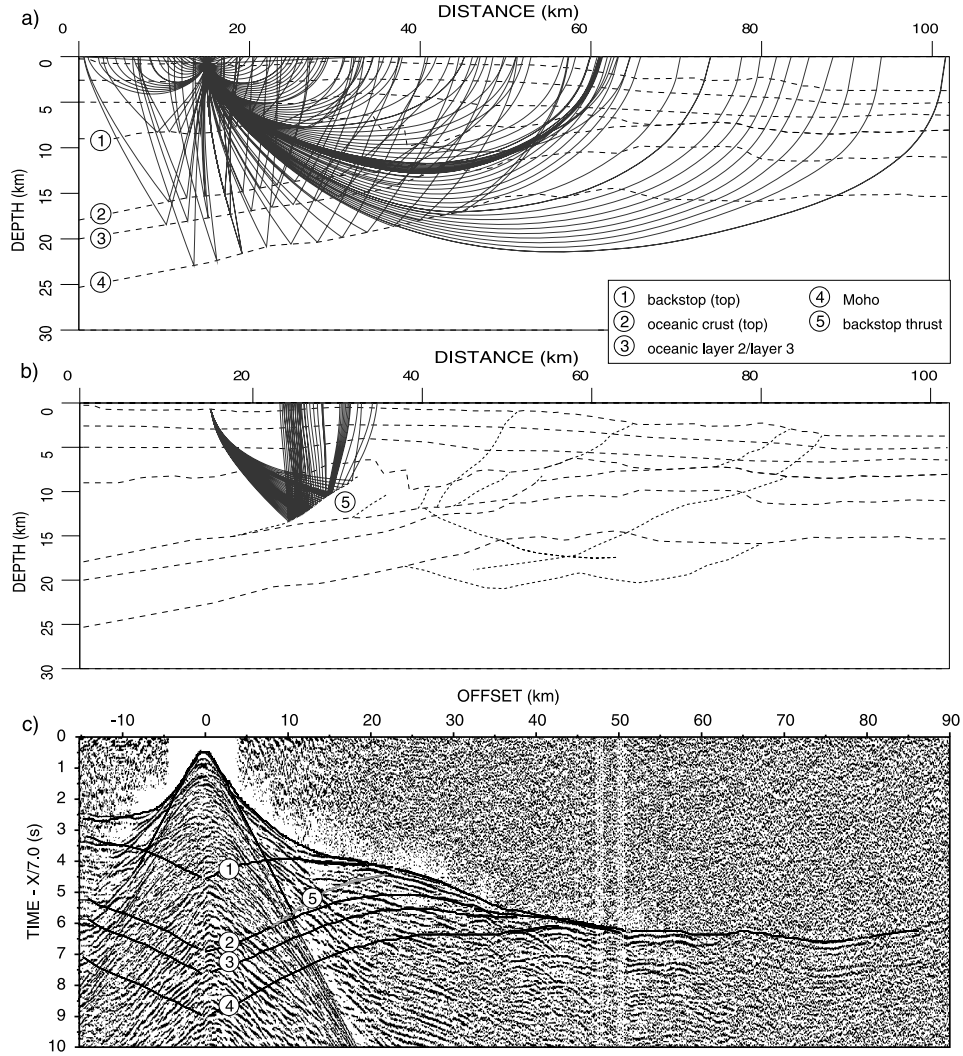

Figure 9. Rays and travel times in the blocky interpretative model for OBS 14. (a) Rays reflected on the major discontinuities, indicated in legend, and turning rays. (b) Rays reflected on the main thrust affecting the backstop. (c) Superposition of data and travel time curves corresponding to the above illustrated ray paths.

discontinuity whose nature is discussed in section 6. Reflections from the lower boundary of a lenticular body at the base of the crust (see Figure 12) that is also discussed further are computed (Figure 10b) too. Here again, the latest computed reflection (corresponding to *PmP*) correlates strongly with data. Some correlation is also noticable for the reflection on the oceanic layer 2/layer 3 discontinuity. Shallower reflectors are somehow harder to correlate unambiguously, considering in particular that the associated arrivals are hardly separable in data. They are, however, found independently by *Martin* [2003] with multichannel seismic data, which confirms their likelihood. Regarding the reflection from the base of the lens, it exhibits slightly different travel times than an otherwise very similar observed arrival (Figure 10c). We calculated the reflection travel times when moving the interpreted reflector 1 km upward and the fit is significantly better (small inset in Figure 10c). The discrepancy probably comes from some limited kinematic mismatch between the smooth and blocky tomographic models. This mismatch is likely to increase when deeper reflectors are considered. Finally, results from OBS 93 give a good correlation for the reflectors associated with the top of the crust and oceanic layer 2/layer 3 transition. Reflections from the Moho appear rather weakly on this recording, except very locally, at critical distance, where they coincide with our computed reflections.

[43] This analysis concerns a few OBSs and shows that some phases in the data correlate well with reconstructed reflectors. For some other reflectors, the correlation is made harder by the complexity of arrivals, caused by the complexity of the medium itself, and the difficulty to separate them. In particular identifying some low amplitude events, only observed on narrow offset ranges, through separate gathers appears very arduous. The migration approach allows us to simultaneously combine data from all OBSs and to extract some information that could most probably not be used with a more classical modeling approach using individual OBSs. Although some of the migrated events are not clearly visible in the data, the validation performed here and the good correlation found for some large reflectors like

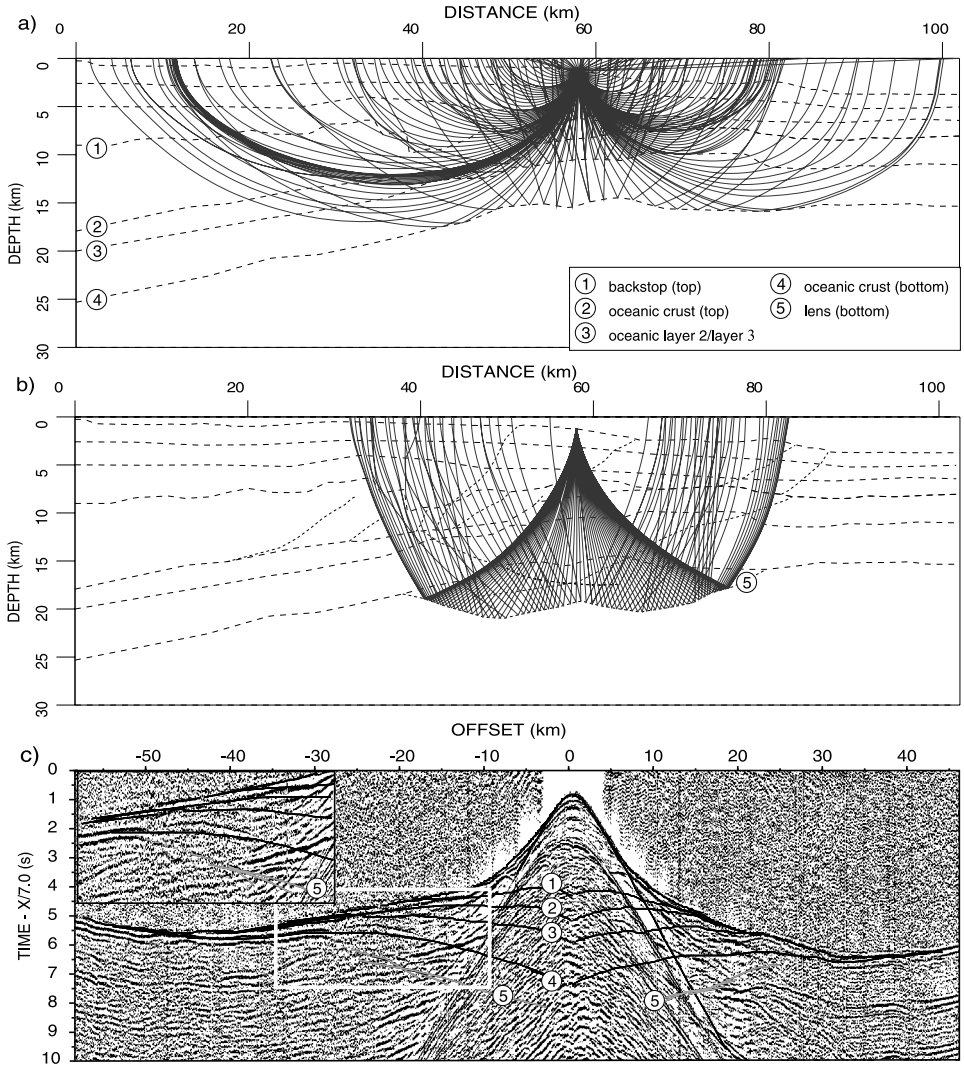

Figure 10. Rays and travel times in the blocky interpretative model for OBS 57. (a) Rays reflected on the major discontinuities, indicated in legend, and turning rays. The shallowest reflection actually corresponds to the bulge-shaped reflector discussed in the text, in direct continuity with the top of the backstop. The bottom of the oceanic crust is not necessarily the Moho here, depending on the nature of the underlying body, discussed in the text. (b) Rays reflected on the bottom of this body. (c) Superposition of data and travel time curves corresponding to the above illustrated ray paths. The inset features the deepest reflection (lens) when the corresponding reflector is moved 1 km upward (see text for details).

the Moho or the top of the backstop make us confident about the migration results and give some credit to our interpretation of structures, presented hereafter.

6. Discussion

[44] Our interpretation of structures, based on our tomographic model (Figure 3b) and on migration results (Figures 8b and 8c), is summarized in Figure 12.

6.1. Subduction Backstop

[45] The most obvious feature appearing in our migrated section is the existence of a large, strong reflector (noted R_{BS} in Figure 8c) between horizontal distances of 15 and 52 km in the model and at depths ranging between 7 and 10 km. This reflector is characterized by a series of marked offsets, the height of which reaches 2.5 km in one case. The reflector thus gradually deepens seaward. This trend is rigorously correlated with the 5 km/s isovelocity curve of our tomographic model in the corresponding area. Also visible in the migration result are $\sim 30^\circ$ tilted reflectors which upper termination coincide with the offsets of the above mentioned large reflector R_{BS}. This undoubtedly demonstrates that important compressive tectonics have affected this unit, which we interpret as the subduction backstop. The tilted reflectors mark the faults along which the compressive deformation was accommodated. The backstop thus appears to have been sliced in the process. Considering the almost completely flat topography above this area, it clearly appears that this deformation pattern is no longer active. The shallower sedimentary layers as they appear in our section and, with a much enhanced resolution,

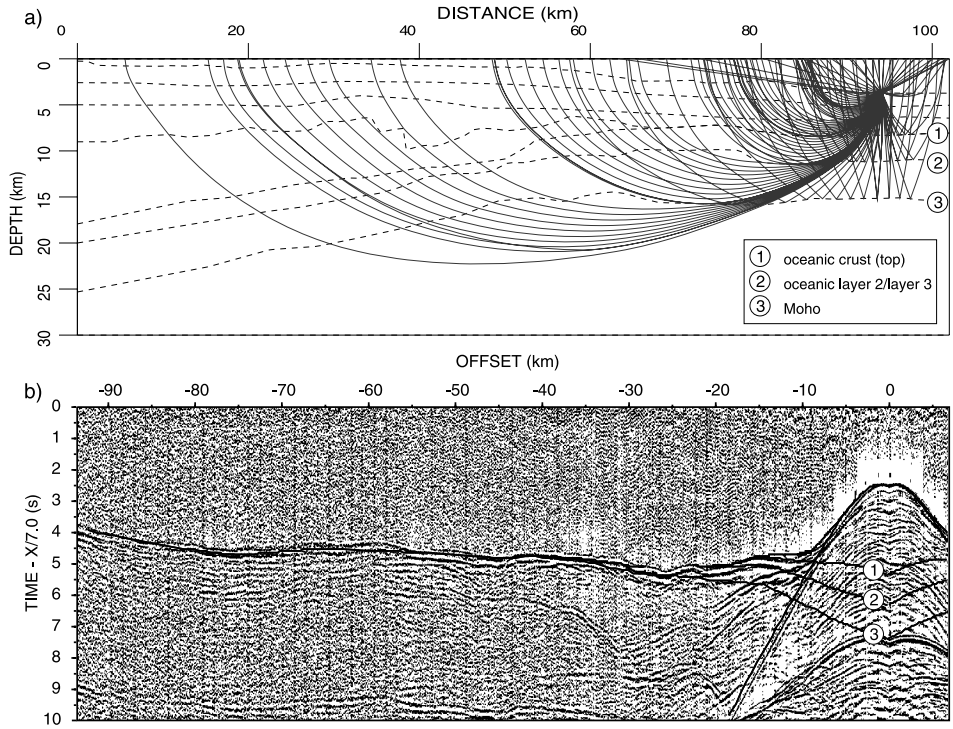

Figure 11. Rays and travel times in the blocky interpretative model for OBS 93. (a) Rays reflected on the major discontinuities, indicated in legend, and turning rays. (c) Superposition of data and travel time curves corresponding to the above illustrated ray paths.

on coincident prestack depth migrated multichannel seismic data [*Martin*, 2003], are flat or very weakly tilted. These sedimentary units have been drilled in a neighboring area by the Japan National Oil Company for the Ministry of International Trade and Industry. The deeper sampled cores (~2200 m below the seafloor) indicate an Eocene age and belong to the Setogawa-Shimanto unit. A stratigraphic correlation of these results on our profile, based on multichannel seismic (MCS) data analysis by *Martin* [2003], indicates that the top of this Eocene unit lies between 2 to 3 km depth.

[46] The reflector R_{BS} appears as a thick event with a long wavelength, like some of the deeper reflectors of our section. Given its relative shallowness, the increase in seismic velocities cannot explain this stretching and we consider this observation as a clear evidence that wide-angle reflections yielded this reflector [*Wu and Toksöz*, 1987]. This diagnosis is further confirmed by the fact that it is not visible on MCS data [*Martin*, 2003], whereas it is very clearly and continuously reconstructed in our section. Two hypotheses could be proposed for this: (1) the reflector could mark a limited impedance contrast between two structural units or (2) it could be a gradational transition in a given unit. In both cases, little or no energy at all would be reflected at short offsets (especially considering that higher frequencies are used in MCS data acquisition),

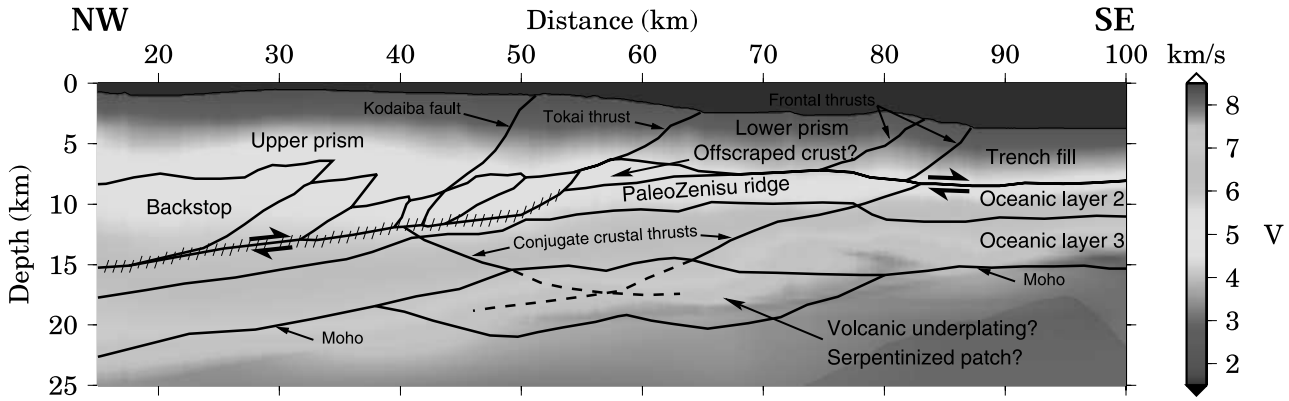

Figure 12. Interpretation of structures along the eastern Nankai subduction. The hachured area represents the upper part of the coseismic slipping zone that is likely to be activated during the next Tokai earthquake. See text for details of the interpretation. See color version of this figure at back of this issue.

whereas reflectivity would be stronger at larger angles. This would in turn imply two hypotheses regarding the backstop: in the first case, its nature would be different than that of the above Eocene sedimentary units, possibly Japanese arc upper igneous crust [*Nakanishi et al.*, 1998, 2002c, 2002d]; in the second case, the whole unit would be constituted by old accreted sediments [*Nakanishi et al.*, 2002a; *Kodaira et al.*, 2003], presumably from the Shimanto belt resulting from the subduction of the Pacific plate beneath the Japanese arc, before the opening of the Philippine Sea plate. Our tomographic model indicates that the velocities below the large reflector range between 5 and 6 km/s, which is in good agreement with those found in corresponding zones on neighboring profiles by *Nakanishi et al.* [1998, 2002b] and *Kodaira et al.* [2003]. It is, however, not possible to discriminate between the two proposed hypotheses on the basis of seismic velocities only. Nevertheless, we consider that the absence of reflected energy at short offsets from this large discontinuity favors the hypothesis of a continuous sedimentary unit. The reflector would therefore consist in a gradient zone that is too narrow to be resolvable by first arrival travel time tomography and too large to yield reflections from a near vertical, high-frequency seismic signal. This gradient zone could be proposed to be associated with a diagenetic front in the Shimanto unit, with possibly a slight metamorphism below it. This would be consistent with heating of the old prism [*Underwood et al.*, 1993] at the onset of the subduction of the young and hot crust of the Philippine Sea plate at 15 Ma [*Aoike*, 1999]. The compressive tectonics offsetting this front would be posterior, possibly corresponding to the strong reactivation of the Philippine/Eurasia convergence at 8 Ma [*Taira*, 2001; *Le Pichon*, 1997] with the accretion of the Tanzawa massif of the Izu-Bonin arc at the collision front [*Niitsuma*, 1989]. Drilling results and stratigraphic correlations by *Martin* [2003] would imply a cessation or at least a strong decrease of this compressive activity in the backstop at early Pliocene.

[47] This compression occurring in the backstop is a likely consequence of the subduction of structural highs carried by the Philippine Sea plate such as that which is discussed in section 6.2. The faulting of the backstop as we observe it therefore provides a mechanism for its retreat as response to subducting crustal topographic highs, as observed in specific areas along the whole Nankai trough by *Nakanishi et al.* [2002a].

6.2. Subducting Ridge

[48] The existence of a subducting ridge below the eastern Nankai trough lower accretionary prism has been discussed for about a decade. The hypothesis was first proposed by *Lallemand et al.* [1992] on the basis of the deformation pattern in the prism and by comparisons with sandbox experiments. It was then further tested by *Le Pichon et al.* [1996a] with gravimetric and magnetic anomalies bringing new evidence. Seismic reflection data results obtained by *Mazzotti et al.* [2002] show the existence of a landward dipping low-angle reflector in the crust that creates a sharp relief in the oceanic basement below the deformation front, which is consistent with compressive tectonics, analogous to that presently observed on the seaward flank of the Zenisu ridge [*Lallemant et al.*, 1989; *Chamot-Rooke and Le Pichon*, 1989]. The analogy in the crustal deformation patterns led to the conclusion that the suspected subducting relief was an equivalent of the Zenisu ridge [*Le Pichon et al.*, 1996a] and is since then known as the "Paleo-Zenisu ridge". However, no direct evidence of the crustal relief had been found from seismic reflection experiments until very recently [*Martin*, 2003], the reflectivity of the top of the oceanic crust being very weak below the accretionary wedge [*Mazzotti et al.*, 2002]. On the other hand, first arrival travel time inversion of OBS data by *Kodaira et al.* [2003] show the existence of a velocity anomaly at the probable location of the subducted ridge.

[49] Our tomographic model, which is based on the same approach as that of *Kodaira et al.* [2003], also clearly shows the existence of a velocity anomaly at the same location with isovelocity curves roughly paralleling the shallowing bathymetry landward, from distances of 50–85 km and at ~6 km depth (Figure 3b). Deeper, a low-velocity anomaly, around 15 km depth, is observable there too. Checkerboard tests show that this zone stands at the limit of the resolved area for 10 km anomalies. The crustal structure can thus be considered reliable and appears to be thicker at the proposed location of the subducting ridge. This is further emphasized by the high-velocity anomaly just seaward. Our migration results convincingly confirm the existence of a non standard oceanic crust in the thickened area. Several features support this observation. Three low-frequency reflectors can be distinguished between ~8 km and ~15 km depth, that we respectively interpret as the top of the oceanic crust, the limit between oceanic layers 2 (basalts) and 3 (gabbro) and the reflector R_M (Figure 8c) that marks the Moho on the seaward end of our profile. Note that the second reflector separating layers 2 and 3 is rather equivocal here, though it is continuous elsewhere. Our interpretation was guided by keeping roughly constant thicknesses for both layers. The reflector R_M does not seem to be underlaid by standard lithospheric mantle throughout the whole profile and therefore can not be interpreted everywhere as the Moho discontinuity, as we shall discuss further. These three reflectors appear to be offset by 1–1.5 km along a 20° reflector (R_{CT1} in Figure 8c) that is coincident with the above mentioned crustal thrust imaged by *Mazzotti et al.* [2002], who estimate a dip of 25°; offsets in subhorizontal reflectors are also visible at corresponding locations in the seismic reflection sections of *Takahashi et al.* [2002]. We, however, note that the reflector associated with the top of the oceanic crust tends to vanish, though not completely disappearing, landward of this thrust. The same can be observed in the coincident multichannel seismic section of *Martin* [2003] and was pointed out by previous studies [*Mazzotti et al.*, 2002]. Actually, beneath the lower prism, this topmost crustal reflector appears as a series of contiguous migration smiles of weak amplitude. A possible explanation for this could be some strong lateral heterogeneities. Considering the Paleo-Zenisu ridge as a subducted equivalent of the present Zenisu ridge, one can assume that the noticable topographic variations observed along the Zenisu ridge (see Figure 1a) are likely to exist on Paleo-Zenisu. Besides, a volcano carried by this ridge and presently impinging the prism is observed immediately westward of our profile through a magnetic anomaly [*Le Pichon et al.*, 1996b], surface deformation pattern [*Mazzotti et al.*, 2002] and

seismic imaging [*Martin*, 2003]. Moreover, the probable presence of volcaniclastic deposits is a further possible cause of weak and poorly coherent reflectivity of the décollement there. However, we consider that the groups of reflectors reconstructed in our migration indicate the upper limit of the subducting oceanic crust. This limit is exactly coincident with that inferred by *Martin* [2003].

[50] Farther landward, between distances of 15–25 km, a strong intracrustal seaward dipping reflector is fairly visible; it is denoted by R_{CT2} in Figure 8c. Its dip is about 20°, as for the landward dipping crustal thrust discussed before, whose associated reflector is not as strong as this one. Likewise, this reflector also coincides at depth with a change in the geometry of the reflector R_M; offsets in upper crustal limits are, however, less obvious. These analogies tend to orient the interpretation of that reflector as a conjugate crustal backthrust, probably of more recent activity. It could also possibly be seen as a normal fault associated with the bending of the plate as it subducts beneath the backstop but this interpretation contradicts the observed style of deformation in the lower part of the crust (reflector R_M). Both interpretations are not completely incompatible since an initially compressive thrust could be reactivated as a normal fault to accommodate recent or present upper crustal extension due to plate bending. Whether or not such an extension has existed, the structure is, however, most probably of compressive origin. In this hypothesis, the thrust and backthrust faults would have created a crustal-scaled pop-up structure that would explain the topography associated with the Paleo-Zenisu ridge. Considering the distance between these two faults at their shallow termination, the width of this topographic high would be ~40 km, which is consistent with that of the Zenisu ridge. Note that such a backthrust affecting the oceanic basement is also observed on the northeastern part of the Zenisu ridge [*Lallemant et al.*, 1989].

[51] The seaward limit of the backstop in our model is located at a distance of 55 km in the model. It apparently marks the landward limit of the topographic elevation associated to the Paleo-Zenisu ridge. Yet, the proposed backthrust, which should mark the landward flank of the subducted ridge, is located some ~12 km farther north. The upper part of the oceanic crust seems to be missing in between. This would imply either that the end of the backstop is actually made of a slice of accreted upper oceanic crust or that this material has been offscraped and underplated beneath the prism, at the top of the subducting ridge and mainly, close to the backstop. We believe that the first hypothesis is unlikely, considering the structural unity of the backstop and its quasi-continuous top at this location. On the other hand, the second one is supported by two observations: a small high-velocity anomaly can be seen in our tomographic model beside the backstop and a coincident reflector delineating a ~10 km large bulge is evidenced in our migration result. This reflector could mark the limit between sediments and offscraped crustal material. The observed volume would roughly balance the missing material beneath the backstop. The Tokai thrust separating the upper and lower parts of the sedimentary wedge would be rooted on the top of this bulge, hence connecting the limit of the backstop as postulated by *Le Pichon et al.* [1996b]. This observation is supported by the results of *Martin* [2003] whose images are sharper and more interpretable than ours in the prism. The décollement is probably duplicated at this location, one part corresponding to the top of the bulge and one part to its bottom. The upper branch could be recent and would have inactivated the Tokai thrust, as is seemingly observed by *Martin* [2003]. Still in relation with the tectonics in the prism, the Kodaiba fault that accommodates a dextral strike-slip motion with a compressive component [*Thoué et al.*, 1995; *Huchon et al.*, 1998] is apparently connected with one of the above described faults affecting the backstop. Note that these faults in the prism appear in our interpreted section (Figure 12) but were actually not inferred from our migration results, which are clearly insufficient for such shallow areas due to acquisition sparsity, but from the results of *Martin* [2003].

[52] The thrust and backsthrust delineating the uplifted oceanic ridge in subduction actually seem to cross the reflector R_M and to flatten and cross each other at about 17 km in depth. One would normally expect that the thrusts affect the entire rigid oceanic lithosphere which is about 30 km thick here [*Chamot-Rooke and Le Pichon*, 1989; *Mazzotti et al.*, 2002]. Although observation of results at depths greater than 15 km is made uncertain by poor imaging conditions and should therefore be taken with care, such lithospheric thrusts are not visible. Actually, a deeper reflector can be observed at 20 km depth and connects with the reflector R_M on both sides of the uplifted area. It thus delineates a ~5 km thick, symmetric lens with the latter. There is some noticable correlation between this lens and the above mentioned low velocity anomaly beneath the Paleo-Zenisu ridge, although this observation should be tempered by the fact that the lens is partially beneath the reliably resolved area (~15 km). The crustal thrusts flatten in this lens suggesting that it is of a more ductile rheology. Two hypotheses can be proposed: this area could consist of underplated volcanic material or a patch of serpentinized mantle. The second solution would be consistent with the lithospheric shortening model of *Mazzotti et al.* [2002] in which a mantle thrust is transferred to a crustal thrust through such a serpentinized patch; this model was proposed for the Zenisu ridge uplift and could therefore be considered for the Paleo-Zenisu ridge as well. However, it requires deeper penetrating thrusts we again have no evidence for. It is also worth mentioning that *Kodaira et al.* [2002] hypothesize the existence of a serpentinized zone underlaid by a reflector beneath a subducting seamount on the western Nankai trough; this supposedly serpentinized area is, however, much thicker in their case (15 km).

[53] The nature of deep crustal materials in the Zenisu and Paleo-Zenisu ridges actually depends on the origin of these tectonic features, and this is not well established. They clearly seem to belong to a series of northeast-southwest trending en échelon ridges that can be observed on the western flank of the Izu-Bonin arc down to 25° latitude [*Karig and Moore*, 1975] and appear to be ancient fracture zones [*Bandy and Hilde*, 1983]. This is supported by an apparent offset in magnetic anomalies observed by *Lallemant et al.* [1989], which besides, confirms that these paleotransform faults affect oceanic crust of the Shikoku Basin. *Mazzotti et al.* [2002] propose that these zones of weakness localize the observed intracrustal compressive deformation as the ridge approaches the subduction front.

This mechanism would in particular explain the presence of serpentinized material through hydration via fluid percolation. On the other hand, several volcanoes can be observed along the Zenisu ridge [*Lallemant et al.*, 1989] and we already mentioned the existence of a buried volcano on the Paleo-Zenisu ridge, next to our profile. This volcanic activity most probably results from the proximity of the ridge with the main Izu-Bonin volcanic arc. It could be argued that crustal weaknesses associated with the en échelon fracture zones result in a migration of magmatism from the main arc, hence the possibility that volcanic material could be underplated beneath the ridges. Two explanations therefore appear equally likely regarding the nature of the lenticular, low-velocity body that is observed below the oceanic layer 3 and that seem to constitute a zone of ductile rheology in an elsewhere rigid lithosphere. Note, however, that one could expect to find serpentinized mantle at shallower depth on a paleotransform fault. Regarding the nature of the reflector R_M at the top of the lens, it could strictly speaking be considered as the Moho in the hypothesis of a serpentinized mantle lens, whereas in the other case of underplated material, it would simply mark the transition with the above oceanic layer 3, the Moho being rather marked by the bottom of the lens. On both sides of this body, the reflector R_M is undoubtedly associated with the Moho.

[54] Landward of the Paleo-Zenisu ridge, the oceanic crust exhibits a more classical structure with an upper layer whose thickness reincreases to ~2 km. The Moho is no longer clearly identifiable but its general trend seems to be parallel to that of the upper boundary of the plate. The total crustal thickness is 7 km, just as it is observed seaward, below the trench fill. The apparent dip of the subduction changes to about 10° beyond the contact with the backstop, which is in agreement with the results of *Nakanishi et al.* [2002b, 2002d]. The plate contact is located at the base of the sliced backstop.

[55] In a subduction context, it is generally considered that the seaward limit of the seismogenic zone in terms of coseismic slip is marked by the end of the mechanical contact between the subducting plate and the backstop [*Brocher et al.*, 1994; *Flueh et al.*, 1998; *Nakanishi et al.*, 2002c]. On the Nankai trough, *Hyndman et al.* [1995] roughly estimate that stable sliding conditions cease about 30 km landward from the trench axis, based on clay transition, in both 1944 and 1946 earthquakes areas. There are strong analogies between the structures described by *Park et al.* [2002] on the segment of the eastern Nankai trough that was ruptured in 1944 and the interpretative model we propose for the adjacent easternmost segment, unruptured since 1854. In particular, they describe an active tsunamigenic splay fault that is quite analogous to the Tokai thrust, although the latter seems to have been recently inactive [*Martin*, 2003]. Their proposed updip limit for the 1944 coseismic slip lies at the branching of this splay fault on the main subduction contact, at ~10 km in depth and 55 km landward of the deformation front. Seaward of this limit, the 1944 coseismic slip would have been partitioned between the splay fault and the plate contact, where it would have ended at the onset of the stable sliding décollement, about 30 km from the trench axis, in agreement with the result of *Hyndman et al.* [1995]. In our case, the branching of the Tokai thrust is observed at a depth of ~9 km and marks the seaward limit of the rigid backstop. The mechanical and thermal conditions are therefore likely to be comparable to those occurring at the main 55 km coseismic slip limit of *Park et al.* [2002], although the distance to the deformation front is only 30 km here. This discrepancy is directly related to the narrowing of the lower accretionary prism observed at the eastern end of the Nankai trough, due to the subduction of topographic features like the Paleo-Zenisu ridge discussed above, as evidenced by *Lallemand et al.* [1992]. Therefore we consider that the updip limit of the potential area of coseismic slip that would be activated in the great earthquake to come on the easternmost segment of the Nankai trough is located some 30 km landward of the deformation front, at a depth of ~9 km, that is, at a position corresponding to the seaward end of the contact between the backstop and the subducting plate (Figure 12). Note that if the observation of *Martin* [2003] about the inactivation of the Tokai thrust happens to be verified, the effects of this next Tokai earthquake should be more limited than what was observed westward in 1944 regarding the triggering of a tsunami since one would expect a weaker vertical coseismic motion if the slip entirely follows the subhorizontal décollement and avoids a steeper splay fault that connects the ocean bottom at relatively low water depth.

[56] One last observation that can be made from our results is that the velocity structure of the subducting crust does not seem to be constant along the model, as often postulated. In particular, the tomographic model seems to indicate lower crustal velocity gradients landward of the Paleo-Zenisu ridge than seaward of it. It is possible that this results from an observational bias due to the loss of resolution in velocities as depth increases; furthermore, the landward area of the subducted ridge stands close to the border limiting the covered area in our model, where checkerboard tests confirm a low resolution of images. However, the hypothesis that increasing temperatures encountered at depth yield a decrease in observed seismic velocities should also be considered as a possible explanation.

7. Conclusions

[57] In this study, we present a two-step seismic imaging approach that is well suited to the particularly dense marine seismic data set we handle. We take advantage of both the wide range of covered offsets and the density of wave field sampling to respectively build a smooth, well-constrained velocity model by inverting first arrival travel times and to reconstruct continuous reflectors with a prestack depth migration. This approach yields an objective tectonic interpretation of structures in that no or very little a priori information is input in the processing of data.

[58] From a tectonic point of view, we obtain new evidences to support a model of steady state deformation pattern with the periodic formation of crustal oceanic ridges [*Le Pichon et al.*, 1996b; *Mazzotti et al.*, 2002; *Kodaira et al.*, 2003] localized along preexisting northeast-southwest weak zones of the Shikoku Basin, on the western flank of the Izu-Bonin arc. These compressive structures result from the necessity of a kinematic transition between a distributed deformation regime in the arc and the rigid adjacent Philippine Sea plate [*Mazzotti et al.*, 1999]. Such a nascent ridge is observed some 50 km south of the Zenisu ridge [*Lallemant et al.*, 1989]; the Zenisu ridge itself represents a

more mature state of these topographic highs. They subsequently enter the subduction where they collide with the backstop and strongly influence the deformation of the eastern Nankai accretionary wedge, the backstop and the oceanic crust itself, as our study proves. In particular, the backstop appears to have been sliced by great thrusts, some of which are relayed in the prism above, whereas the subducting oceanic crust exhibits a pop-up structure responsible for the formation of the crustal topographic high known as the Paleo-Zenisu ridge, that is presently in contact with the backstop and probably gets partially offscraped in the process. This kind of elongated trench-parallel topographic feature is furthermore quite likely to represent a strong coupling factor that could be related with the segmentation of the trough, since the postulated extent of the Paleo-Zenisu ridge coincides with the unruptured easternmost segment of the Nankai subducting system [*Nakanishi et al.*, 2002b]. Deeper, a zone of relatively low velocity delineated by a reflector is observed. It probably consists of a soft rheology zone in which the intracrustal conjugate thrusts flatten and seemingly die out. This zone is proposed to be made of either underplated volcanic material or of serpentinized upper mantle, both hypotheses being compatible with what is presently known of the northeast-southwest trending crustal weaknesses that presumably localize intraoceanic compressive deformation.

[59] This new type of seismic acquisition presents a promising perspective for much improved deep crustal studies, both qualitatively and quantitatively. From a data processing aspect, 2-D full wave field inversion approaches [*Pratt et al.*, 1996] could be investigated as a complement to travel time tomography for quantifying the model properties over a complete range of accessible wavelengths.

[60] **Acknowledgments.** We had many interesting and instructive discussions during the buildup of this study. We thus thank P. Henry, S. Lallemant, V. Martin, P. Huchon, N. Chamot-Rooke, S. Mazzotti, H. Tokuyama, K. Suyehiro, A. Taira, I. Aki, J.-Y. Collot, P. Charvis, M.-O. Beslier, D. Graindorge, and J. Virieux for their help and suggestions. We also thank the scientific and technical boarding crew of the R/V *Kaiyo* in charge of data acquisition. The French side particularly thanks B. Hustedt for his participation in this campaign. The eikonal solver used in our modeling of first arrival travel times was taken from the FAST package [*Zelt and Barton*, 1998]. The RAYINVR software of *Zelt and Smith* [1992] was used for both constructing an initial model for our first arrival travel time tomography and for modeling refracted and reflected phases in our checking of migration results. GMT software [*Wessel and Smith*, 1995] was used to prepare some of the figures in the paper. J.-X. Dessa's postdoctoral fellowship is funded through a contract with the Centre National de la Recherche Scientifique. We finally thank two anonymous reviewers for constructive comments. This paper is contribution 631 of the UMR Géosciences-Azur.

References

Ando, M. (1975a), Possibility of a major earthquake in the Tokai district, Japan and its pre-estimated seismotectonic effects, *Tectonophysics*, *25*, 69–85.

Ando, M. (1975b), Source mechanisms and tectonic significance of historical earthquakes along the Nankai trough, Japan, *Tectonophysics*, *27*, 119–140.

Ando, M. (1982), A fault model of the 1946 Nankaido earthquake derived from tsunami data, *Phys. Earth Planet. Inter.*, *28*, 320–336.

Aoike, K. (1999), Tectonic evolution of the Izu collision zone, (in Japanese) *Res. Rep.*, *9*, 113–151, Kanagawa Prefectural Mus. Nat. Hist., Odawara, Japan.

Baba, T., Y. Tanioka, P. R. Cummins, and K. Uhira (2002), The slip distribution of the 1946 Nankai earthquake estimated from tsunami inversion using a new plate model, *Phys. Earth Planet. Inter.*, *132*, 59–73.

Bandy, W. L., and T. W. C. Hilde (1983), Structural features of the Bonin arc: Implications for its tectonic history, *Tectonophysics*, *99*, 331–353.

Brocher, T. M., G. S. Fuis, M. A. Fisher, G. Plafker, M. J. Moses, J. J. Taber, and N. I. Christensen (1994), Mapping the megathrust beneath the northern Gulf of Alaska using wide-angle seismic data, *J. Geophys. Res.*, *99*, 11,663–11,685.

Chamot-Rooke, N., and X. Le Pichon (1989), Zenisu ridge: Mechanical model of formation, *Tectonophysics*, *160*, 175–193.

Cummins, P. R., T. Baba, S. Kodaira, and Y. Kaneda (2002), The 1946 Nankai earthquake and segmentation of the Nankai trough, *Phys. Earth Planet. Inter.*, *132*, 75–87.

Fliedner, M. M., and R. S. White (2003), Depth imaging of basalt flows in the Faeroe-Shetland Basin, *Geophys. J. Int.*, *152*, 353–371.

Flueh, E. R., N. Vidal, C. R. Ranero, A. Hojka, R. von Huene, J. Bialas, K. Hinz, D. Cordoba, J. J. Dañobeitia, and C. A. Zelt (1998), Seismic investigation of the continental margin off- and onshore Valparaiso, Chile, *Tectonophysics*, *288*, 251–263.

Hearn, T. M., and J. F. Ni (1994), P_n velocities beneath continental collision zones: The Turkish-Iranian Plateau, *Geophys. J. Int.*, *117*, 273–283.

Henry, P., S. Mazzotti, and X. Le Pichon (2001), Transient and permanent deformation of central Japan estimated by GPS, 1. Interseismic loading and subduction kinematics, *Earth Planet. Sci. Lett.*, *184*, 443–453.

Holbrook, W. S., E. C. Reiter, G. M. Purdy, D. Sawyer, P. L. Stoffa, J. A. Austin, J. Oh, and J. Makris (1994), Deep structure of the U.S. Atlantic continental margin, offshore South Carolina, from coincident ocean bottom and multichannel seismic data, *J. Geophys. Res.*, *99*, 9155–9178.

Hole, J. A., and B. C. Zelt (1995), 3-D finite-difference reflection traveltimes, *Geophys. J. Int.*, *121*, 427–434.

Huchon, P., and H. Kitazato (1984), Collision of the Izu block with Central Japan during the Quaternary and geologic evolution of the Ashigara area, *Tectonophysics*, *110*, 201–210.

Huchon, P., H. Tokuyama, S. J. Lallemant, A. Taira, P. Henry, S. Mazzotti, X. Le Pichon, and the KAIKO-TOKAI'96 on Board Scientific Party (1998), Pervasive dextral strike-slip faulting within the backstop of the eastern Nankai wedge confirmed by deep-towed seismic data (*Kaiko*-TOKAI'96 cruise), *C. R. Acad. Sci.*, *326*, 869–875.

Hyndman, R. D., K. Wang, and M. Yamano (1995), Thermal constraints on the seismogenic portion of the southwestern Japan subduction thrust, *J. Geophys. Res.*, *100*, 15,373–15,392.

Ishida, M. (1992), Geometry and relative motion of the Philippine Sea plate and Pacific plate beneath the Kanto-Tokai district, Japan, *J. Geophys. Res.*, *97*, 489–513.

Jin, S., R. Madariaga, J. Virieux, and G. Lambaré (1992), Two-dimensional asymptotic iterative elastic inversion, *Geophys. J. Int.*, *108*, 575–588.

Kanamori, H. (1972), Tectonic implications of the 1944 Tonankai and 1946 Nankaido earthquakes, *Phys. Earth Planet. Inter.*, *5*, 129–139.

Karig, D. E., and G. F. Moore (1975), Tectonic complexities in the Bonin arc system, *Tectonophysics*, *27*, 97–118.

Kodaira, S., N. Takahashi, A. Nakanishi, S. Miura, and Y. Kaneda (2000), Subducted seamount imaged in the rupture zone of the 1946 Nankaido earthquake, *Science*, *289*, 104–106.

Kodaira, S., E. Kurashimo, J.-O. Park, N. Takahashi, A. Nakanishi, S. Miura, T. Iwasaki, N. Hirata, K. Ito, and Y. Kaneda (2002), Structural factors controlling the rupture process of a megathrust earthquake at the Nankai trough seismogenic zone, *Geophys. J. Int.*, *149*, 815–835.

Kodaira, S., A. Nakanishi, J.-O. Park, A. Ito, T. Tsuru, and Y. Kaneda (2003), Cyclic ridge subduction at an inter-plate locked zone off central Japan, *Geophys. Res. Lett.*, *30*(6), 1339, doi:10.129/2002GL016595.

Korenaga, J., W. S. Holbrook, G. M. Kent, P. B. Kelemen, R. S. Detrick, H.-C. Larsen, J. R. Hopper, and T. Dahl-Jensen (2000), Crustal structure of the southeast Greenland margin from joint refraction and reflection seismic tomography, *J. Geophys. Res.*, *105*, 21,591–21,614.

Kumagai, H. (1996), Time sequence and the recurrence models for large earthquakes along the Nankai trough revisited, *Geophys. Res. Lett.*, *23*, 1139–1142.

Lafond, C. F., and A. Levander (1995), Migration of wide-aperture onshore-offshore seismic data, central California: Seismic images of late stage subduction, *J. Geophys. Res.*, *100*, 22,231–22,243.

Lallemant, S., N. Chamot-Rooke, X. Le Pichon, and C. Rangin (1989), Zenisu Ridge: A deep intraoceanic thrust related to subduction, off southwest Japan, *Tectonophysics*, *160*, 151–174.

Lallemand, S., J. Malavieille, and S. Calassou (1992), Effects of oceanic ridge subduction on accretionary wedges: Experimental modeling and marine observations, *Tectonics*, *11*, 1301–1313.

Lambaré, G., P. S. Lucio, and A. Hanyga (1996), Two-dimensional multivalued traveltime and amplitude maps by uniform sampling of ray field, *Geophys. J. Int.*, *125*, 584–598.

Le Pichon, X. (1997), La déformation du Japon, cours, Coll. de France, Paris.

Le Pichon, X., F. Pollitz, M. Fournier, J.-P. Cadet, S. Lallemant, and N. Chamot-Rooke (1996a), Distribution of shortening landward and oceanward of the eastern Nankai trough due to the Izu-Ogasawara ridge collision, *Earth Planet. Sci. Lett.*, *137*, 145–156.

Le Pichon, X., S. Lallemant, H. Tokuyama, F. Thoué, P. Huchon, and P. Henry (1996b), Structure and evolution of the backstop in the eastern Nankai Trough area (Japan): Implications for the soon-to-come Tokai earthquake, *Island Arc*, *5*, 440–454.

Martin, V. (2003), Structure et tectonique du prisme d'accrétion de Nankai dans la zone Tokai par imagerie sismique en trois dimensions, Ph.D. thesis, Univ. Paris XI, Orsay, France.

Mazzotti, S. (1999), L'arc insulaire japonais: Déformation transitoire et permanente liée à la subduction et à la collision, Ph.D. thesis, Univ. Paris XI, Orsay, France.

Mazzotti, S., P. Henry, X. Le Pichon, and T. Sagiya (1999), Strain partitioning in the zone of transition from Nankai subduction to Izu-Bonin collision (Central Japan): Implications for an extensional tear within the subducting slab, *Earth Planet Sci. Lett.*, *172*, 1–10.

Mazzotti, S., X. Le Pichon, P. Henry, and S. Miyazaki (2000), Full interseismic locking of the Nankai and Japan-west Kurile subduction zones: An analysis of uniform elastic strain accumulation in Japan constrained by permanent GPS, *J. Geophys. Res.*, *105*, 13,159–13,177.

Mazzotti, S., P. Henry, and X. Le Pichon (2001), Transient and permanent deformation of central Japan estimated by GPS, 2. Strain partitioning and arc-arc collision, *Earth Planet. Sci. Lett.*, *184*, 455–469.

Mazzotti, S., S. Lallemant, P. Henry, X. Le Pichon, H. Tokuyama, and N. Takahashi (2002), Intraplate shortening and underthrusting of a large basement ridge in the eastern Nankai subduction zone, *Mar. Geol.*, *187*, 63–88.

McIntosh, K., et al. (2000), Large aperture seismic imaging at a convergent margin: Techniques and results from the Costa Rica seismogenic zone, *Mar. Geophys. Res.*, *21*, 451–474.

McMechan, G. A., and G. S. Fuis (1987), Ray equation migration of wide-angle reflections from southern Alaska, *J. Geophys. Res.*, *92*, 407–420.

Milkereit, B., D. Epili, A. G. Green, R. F. Mereu, and P. Morel-à-l'Huissier (1990), Migration of wide-angle seismic reflection data from the Grenville front in Lake Huron, *J. Geophys. Res.*, *95*, 10,987–10,998.

Mochizuki, K., G. Fujie, T. Sato, J. Kasahara, R. Hino, M. Shinoara, and K. Suyehiro (1998), Heterogeneous crustal structure across a seismic block boundary along the Nankai trough, *Geophys. Res. Lett.*, *25*, 2301–2304.

Nakanishi, A., H. Shiobara, R. Hino, S. Kodaira, T. Kanazawa, and H. Shimamura (1998), Detailed subduction structure across the eastern Nankai trough obtained from ocean bottom seismographic profiles, *J. Geophys. Res.*, *103*, 27,151–27,168.

Nakanishi, A., S. Kodaira, J.-O. Park, and Y. Kaneda (2002a), Deformable backstop as seaward end of coseismic slip in the Nankai trough seismogenic zone, *Earth Planet. Sci. Lett.*, *203*, 255–263.

Nakanishi, A., H. Shiobara, R. Hino, J. Kasahara, K. Suyehiro, and H. Shimamura (2002b), Crustal structure around the eastern end of coseismic rupture zone of the 1944 Tonankai earthquake, *Tectonophysics*, *354*, 257–275.

Nakanishi, A., N. Takahashi, J.-O. Park, S. Miura, S. Kodaira, Y. Kaneda, N. Hirata, T. Iwasaki, and M. Nakamura (2002c), Crustal structure across the coseismic rupture zone of the 1944 Tonankai earthquake, the central Nankai trough seismogenic zone, *J. Geophys. Res.*, *107*(B1), 2007, doi:10.129/2001JB000424.

Nakanishi, A., et al. (2002d), Deep crustal structure of the eastern Nankai trough and Zenisu ridge by dense airgun-OBS seismic profiling, *Mar. Geol.*, *187*, 47–62.

Niitsuma, N. (1989), Collision tectonics in the southern Fossa Magna, central Japan, *Mod. Geol.*, *14*, 3–18.

Obana, K., S. Kodaira, K. Mochizuki, and M. Shinoara (2001), Microseismicity around the seaward updip limit of the 1946 Nankai earthquake dislocation area, *Geophys. Res. Lett.*, *28*, 2333–2336.

Paige, C. C., and M. A. Saunders (1982), LSQR: An algorithm for sparse linear equations and sparse least squares, *Trans. Math. Software*, *8*, 43–71.

Park, J.-O., T. Tsuru, S. Kodaira, P. R. Cummins, and Y. Kaneda (2002), Splay fault branching along the Nankai subduction zone, *Science*, *297*, 1157–1160.

Podvin, P., and I. Lecomte (1991), Finite difference computation of traveltimes in very contrasted velocity models: A massively parallel approach and its associated tools, *Geophys. J. Int.*, *105*, 271–284.

Pratt, R. G., Z.-M. Song, P. R. Williamson, and M. Warner (1996), Two-dimensional velocity models from wide-angle seismic data by wavefield inversion, *Geophys. J. Int.*, *124*, 323–340.

Sagiya, T. (1999), Interplate coupling in the Tokai District, central Japan, deduced from continuous GPS data, *Geophys. Res. Lett.*, *26*, 2315–2318.

Sagiya, T., and W. Thatcher (1999), Coseismic slip resolution along a plate boundary megathrust: The Nankai trough, southwest Japan, *J. Geophys. Res.*, *104*, 1111–1129.

Satake, K. (1993), Depth distribution of coseismic slip along the Nankai trough, Japan, from joint inversion of geodetic and tsunami data, *J. Geophys. Res.*, *98*, 4553–4565.

Sato, T., K. Mochizuki, J. Kasahara, G. Fujie, H. Nishisaka, and S. Koresawa (1998), Depth variation of the crustal structure of the subducting plate along the Nankai trough, off Kii Channel, Japan, *Geophys. Res. Lett.*, *25*, 4011–4014.

Seno, T., S. Stein, and A. E. Gripp (1993), A model for the motion of the Philippine Sea plate consistent with NUVEL-1 and geologic data, *J. Geophys. Res.*, *98*, 17,941–17,948.

Shinohara, M., K. Suyehiro, S. Matsuda, and K. Ozawa (1993), Digital recording of ocean bottom seismometer using portable digital audio tape recorder (in Japanese with English abstract), *J. Jpn. Soc. Mar. Surveys Technol.*, *5*, 21–31.

Simon, M., H. Gebrande, and M. Bopp (1996), Pre-stack migration and true-amplitude processing of DEKORP near-normal incidence and wide-angle reflection measurements, *Tectonophysics*, *264*, 381–392.

Taira, A. (2001), Tectonic evolution of the Japanese island arc system, *Annu. Rev. Earth Planet. Sci.*, *29*, 109–134.

Taira, A., H. Tokuyama, and W. Soh (1989), Accretion tectonics and evolution of Japan, in *The Evolution of the Pacific Ocean Margins*, edited by Z. Ben-Avraham, pp. 100–123, Oxford Univ. Press, New York.

Takahashi, N., H. Amano, K. Hirata, H. Kinoshita, S. Lallemant, H. Tokuyama, F. Yamamoto, A. Taira, and K. Suyehiro (2002), Faults configuration around the eastern Nankai trough deduced by multichannel seismic profiling, *Mar. Geol.*, *187*, 31–46.

Tanioka, Y., and K. Satake (2001), Detailed coseismic slip distribution of the 1944 Tonankai earthquake estimated from tsunami waveforms, *Geophys. Res. Lett.*, *28*, 1075–1078.

Tarantola, A. (1987), *Inverse Problem Theory: Methods for Data Fitting and Model Parameter Estimation*, Elsevier Sci., New York.

Thatcher, W. (1984), The earthquake deformation cycle at the Nankai trough, southwest Japan, *J. Geophys. Res.*, *89*, 3087–3101.

Thierry, P., S. Operto, and G. Lambaré (1999), Fast 2-D ray + Born inversion/migration in complex media, *Geophysics*, *64*, 162–181.

Thoué, F., P. Huchon, and K. Kobayashi (1995), Structural style of the 34°15′N, 138°10′E depression on the middle slope of the eastern Nankai trough (October 1994, Shinkai 2000 dives), *JAMSTEC J. Deep Sea Res.*, *11*, 197–204.

Thurber, C. H. (1983), Earthquake locations and three-dimensional crustal structure in the Coyote Lake area, central California, *J. Geophys. Res.*, *88*, 8226–8236.

Toomey, D. R., S. C. Solomon, and G. M. Purdy (1994), Tomographic imaging of the shallow crustal structure of the East Pacific Rise at 9°30′N, *J. Geophys. Res.*, *99*, 24,135–24,157.

Underwood, M. B., T. Byrne, J. Hibbard, L. DiTullio, and M. Laughland (1993), The effects of ridge subduction on the thermal structure of accretionary prisms: A Tertiary example from the Shimanto Belt of Japan, in *Thermal Evolution of the Tertiary Shimanto Belt, Southwest Japan: An Example of Ridge-Trench Interaction*, edited by M. B. Underwood, *Spec. Pap. Geol. Soc. Am.*, *273*, 151–168.

Vidale, J. E. (1988), Finite difference calculation of travel times, *Bull. Seismol. Soc. Am.*, *78*, 2062–2076.

Wessel, R. S., and W. H. F. Smith (1995), New version of the generic mapping tool (GMT) version 3.0 released, *Eos Trans. AGU*, *76*, 329.

Williamson, P. R. (1991), A guide to the limits of resolution imposed by scattering in ray tomography, *Geophysics*, *56*, 202–207.

Wu, R., and M. N. Toksöz (1987), Diffraction tomography and multisource holography applied to seismic imaging, *Geophysics*, *52*, 11–25.

Yamazaki, T., and Y. Okamura (1989), Subducting seamounts and deformation of overriding forearc wedges around Japan, *Tectonophysics*, *160*, 207–229.

Zelt, B. C., M. Talwani, and C. A. Zelt (1998), Prestack depth migration of dense wide-angle seismic data, *Tectonophysics*, *286*, 193–208.

Zelt, C. A., and P. J. Barton (1998), Three-dimensional seismic refraction tomography: A comparison of two methods applied to data from the Faeroe Basin, *J. Geophys. Res.*, *103*, 7187–7210.

Zelt, C. A., and R. B. Smith (1992), Seismic travel time inversion for 2-D crustal velocity structure, *Geophys. J. Int.*, *108*, 16–34.

J.-X. Dessa and S. Operto, Géosciences Azur, CNRS UMR 6526, Observatoire Océanologique de Villefranche, La Darse, BP 48, 06230 Villefranche-sur-Mer, France. (jxdessa@obs-vlfr.fr)

Y. Kaneda, S. Kodaira, and A. Nakanishi, Institute for Frontier Research on Earth Evolution, Japan Marine Science and Technology Center, Showamachi 3175-25, Kanazawa-ku, Yokohama 236-0001, Japan.

G. Pascal, Laboratoire de Géologie, CNRS UMR 8538, École Normale Supérieure, 24 rue Lhomond, 75231 Paris cedex 05, France.

K. Uhira, Japan Meteorological Agency, 1-3-4 Ote-machi, Chiyoda-ku, Tokyo 100-8122, Japan.

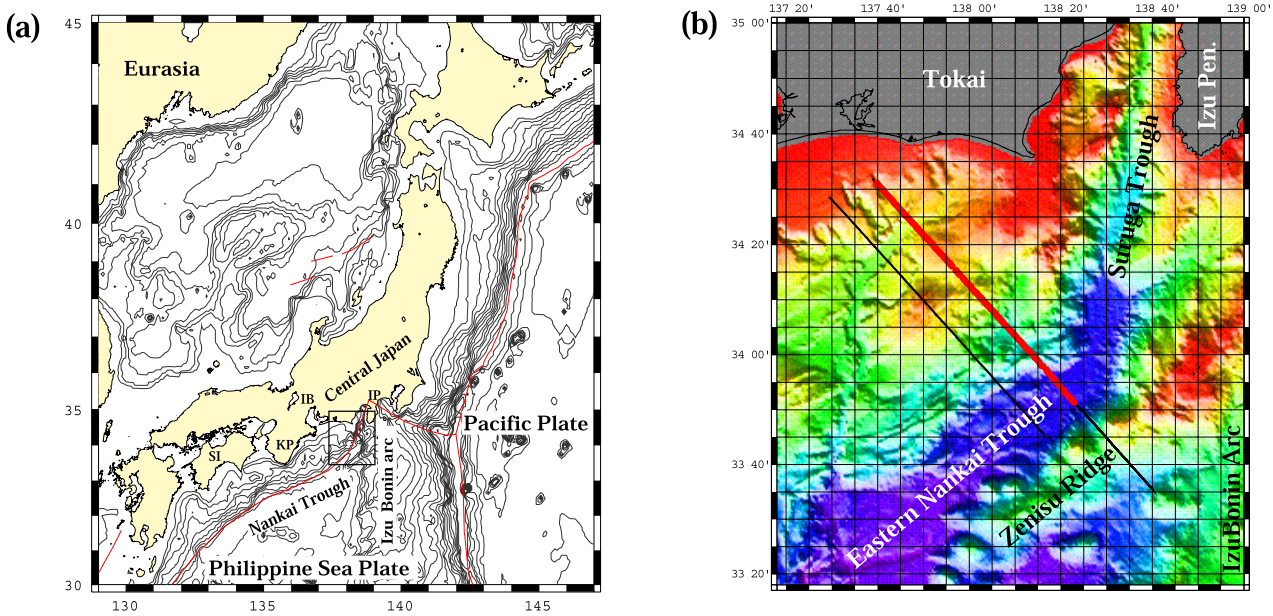

Figure 1. (a) General geodynamic setting around the Nankai trough (map after *Mazzotti* [1999]). Places referred to in the text as Shikoku Island, Kii Peninsula, Ise Bay, and Izu Peninsula are denoted SI, KP, IB, and IP, respectively. (b) Zoom of box shown in Figure 1a with the main structures of the survey area. The two straight black lines denote the shot profiles acquired during the survey; only data from the easternmost one are considered in this study. The thicker and shorter line superimposed on it corresponds to the OBS array.

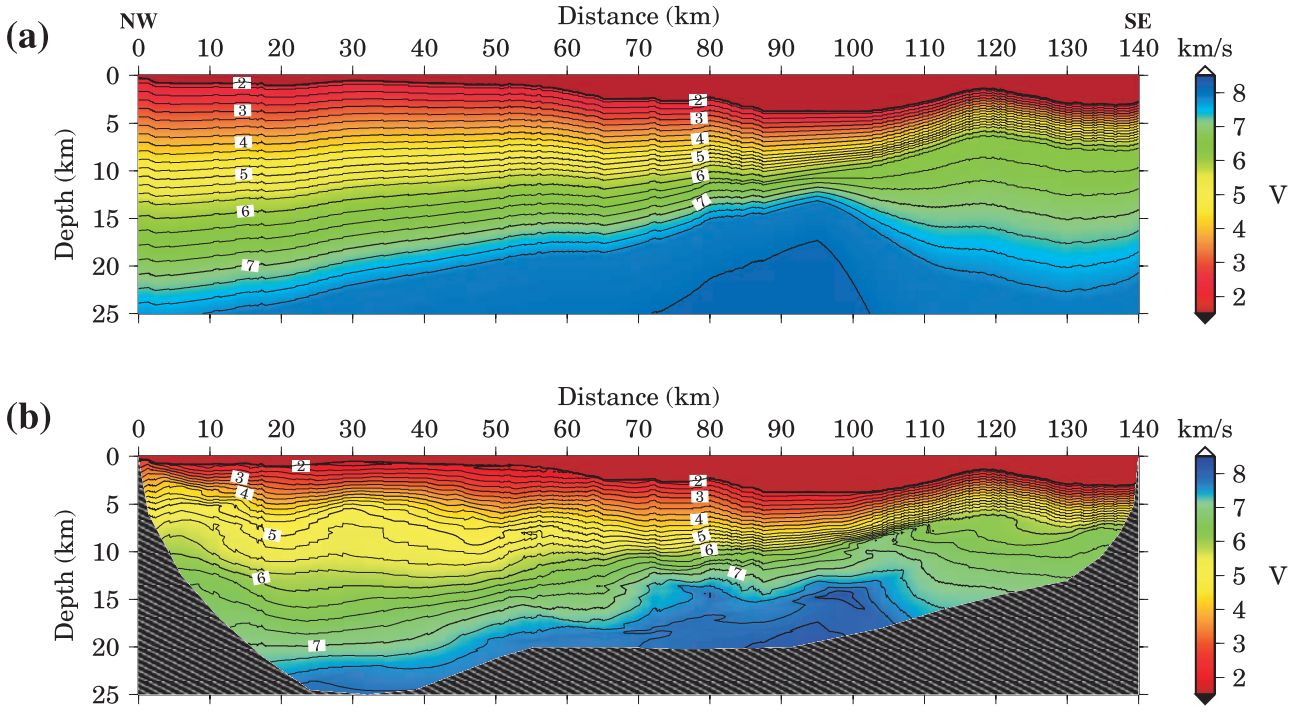

Figure 3. Result of tomographic inversion. (a) Starting model. (b) Corresponding output. The hachured pattern corresponds to unconstrained areas that are not covered by ray paths.

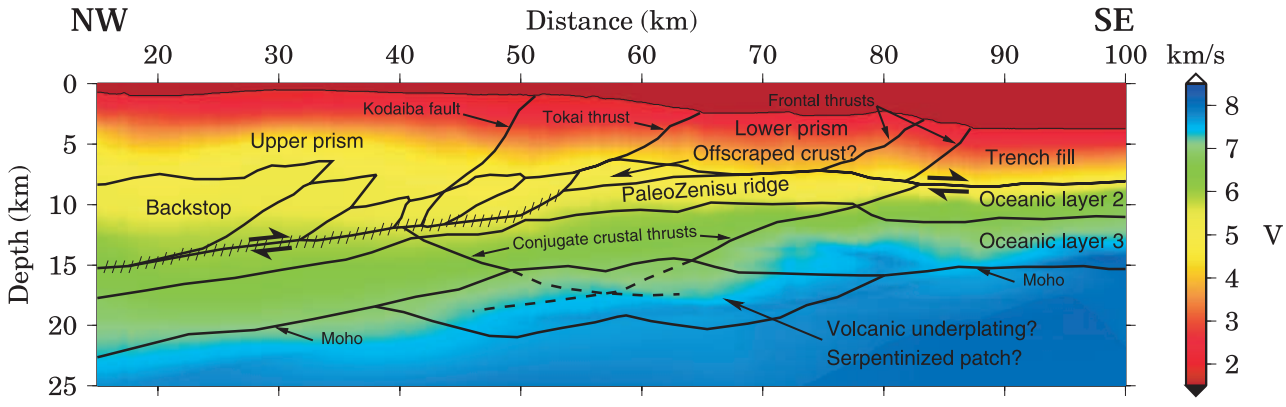

Figure 12. Interpretation of structures along the eastern Nankai subduction. The hachured area represents the upper part of the coseismic slipping zone that is likely to be activated during the next Tokai earthquake. See text for details of the interpretation.